ORNL-3692
UC-34 – Physics
TID-4500 (32nd ed.)

CORRELATED ENERGY AND TIME-OF-FLIGHT MEASUREMENTS OF FISSION FRAGMENTS

(Thesis)

W. E. Kiker

OAK RIDGE NATIONAL LABORATORY
operated by
UNION CARBIDE CORPORATION
for the
U.S. ATOMIC ENERGY COMMISSION

Printed in USA. Price $2.00. Available from the
Office of Technical Services
U. S. Department of Commerce
Washington 25, D. C.

ORNL-3692

Contract No. W-7405-eng-26

Physics Division

CORRELATED ENERGY AND TIME-OF-FLIGHT MEASUREMENTS OF FISSION FRAGMENTS

W. E. Kiker

Submitted as a thesis to the Graduate Council of The University of Tennessee in partial fulfillment of the requirements for the degree of Doctor of Philosophy

OCTOBER 1964

OAK RIDGE NATIONAL LABORATORY
Oak Ridge, Tennessee
operated by
UNION CARBIDE CORPORATION
for the
U.S. ATOMIC ENERGY COMMISSION

ACKNOWLEDGMENTS

The author is indebted to Dr. H. W. Schmitt who suggested the problem and gave much assistance and encouragement and to Dr. R. W. Lide for many enlightening discussions.

Particular thanks are due the Physics Department and Graduate School of the University of Tennessee, Deans A. H. Nielsen and Hilton Smith, the Oak Ridge National Laboratory, and the Oak Ridge Institute of Nuclear Studies for the Oak Ridge Graduate Fellowship that furnished financial support during this experiment.

Notes of appreciation are also due Mr. R. H. Ward, whose engineering know-how contributed so heavily to the successful completion of the experiment, Mr. C. W. Williams, who developed most of the electronics, and Mrs. Ruby Burrell, who typed the manuscript.

TABLE OF CONTENTS

LIST OF FIGURES

FIGURE PAGE

CHAPTER I

INTRODUCTION

I. A BRIEF REVIEW OF FISSION

Discovery and Early Experiments

The first evidence for the existence of nuclear fission was presented by the German radiochemists, Hahn and Strassman (1939a, 1939b). They showed that the radioactive elements formed in the bombardment of uranium by neutrons were not transuranium elements, as had been believed, but were medium weight isotopes. This finding was immediately interpreted by Meitner and Frisch (1939) as the breaking up of an excited uranium nucleus into two particles of medium weight. A consideration of the mass deficiences of the elements in the periodic table led these authors to recognize that very large amounts of energy should be released in fission. Frisch (1939) and Joliot (1939) demonstrated this large energy release experimentally by ionization chamber and range measurement techniques, respectively.

Energy Measuring Experiments

Quantitative ion chamber measurements on the kinetic energy of fission fragments gave the first evidence of the asymmetric nature of fission. Jentschke and Prankl (1939) showed that there is a low energy group centered at about 60 MeV and a high energy group at about 100 MeV. The mass asymmetry has been verified by many radiochemical (Thode and Graham, 1947; Glendenin, Steinberg, Inghram and Hess, 1951) and mass spectrographic (Thode, 1960) measurements.

Brunton and Hanna (1950), and Brunton and Thompson (1950) made correlated energy measurements by means of back to back ionization chambers. In principle, they were able to obtain such kinetic parameters as total fragment kinetic energy and fragment mass distributions. However, the energies obtained were in significant disagreement with calorimetric values by Henderson (1940) and later by Leachman and Shafer (1955). The mass distributions also failed to agree with radiochemical results. These discrepancies were later shown to be due to the so-called "ionization defect"; the difference between the average energy per ion pair expended by alpha particles and by fission fragments. This effect was suggested by Knipp and Ling (1951) and demonstrated experimentally by Leachman and Schmitt (1954) and Schmitt and Leachman (1956).

The latest experimental device for measuring charged particle energies is the solid-state detector. Extensive energy correlation data have been obtained by Schmitt and his co-workers at Oak Ridge National Laboratory (Schmitt, Neiler, Walter, and Chetham-Strode, 1962; Walter, Schmitt, and Neiler, 1964). Unfortunately, there were again, some discrepancies between energies measured by this method and by conversion of some time-of-flight data to energy units. Extensive studies of the pulse-height vs. energy relation in solid-state detectors is presently underway at this laboratory.

Time-of-Flight Measurements

Time-of-flight measurements on fission fragments were first made by Leachman (1952) in an attempt to reconcile the differences between correlated ion chamber measurements and other experiments. This work led to the finding of the above mentioned ionization defect.

Time-of-flight studies were extended to include correlated measurements in which the velocity of each fragment was measured. Several careful and elaborate double time-of-flight experiments have been reported (for instance, see Stein and Whetstone, 1958; Milton and Fraser, 1962; Whetstone, 1963).

II. PURPOSE OF THIS RESEARCH

As was pointed out above, there is a wealth of experimental data available on nuclear fission. However, fission is a complicated process. Considering only binary fission, in order to describe one fission event, it is necessary to state the mass split of the initial nucleus; the charge split; the kinetic energies of the fragments; the numbers and energies of the gamma rays from each fragment; and the angular momenta of the fragments. In addition one must consider the initial mass, charge, and energy state of the fissioning nucleus. This, added to the fact that much of the available data has been rendered virtually obsolete by recent improvements in experimental technique and data processing, makes any carefully obtained experimental data worthwhile in its own right. However, this work was done with several specific objectives in mind.

The first was to obtain a kinetically determined post-neutron mass distribution. (Throughout this work the terms "pre-neutron" and "post-neutron" will refer to kinetic parameters before and after the emission of the so-called "prompt" neutrons, the neutrons emitted by the fission fragments within about 10^{-14} seconds after scission.) The mass distributions from double time-of-flight measurements are

pre-neutron distributions, even though the fragment flight times are much longer than the neutron emission time. This is because the data analysis is based on conservation of momentum, which must be applied before the perturbing effect of neutron emission. This is accomplished by assuming that the neutron emission in the center of mass system of each fragment is symmetric with respect to a plane perpendicular to the direction of motion of the fragment. Then the measured velocities are the same, on the average, as the velocities before neutron emission, and pre-neutron kinetic parameters are obtained. The analysis of energy correlation data is even more involved and the resulting mass distributions are approximately pre-neutron distributions. On the other hand, the radiochemical mass determinations are not effected by prompt neutron emission and are post-neutron distributions and, therefore, compare with the available kinetically determined mass distributions only through the function, $\bar{\nu}(M)$, the average number of prompt neutrons emitted as a function of fragment mass. A correlated measurement of the energies and times-of-flight of single fission fragments, made after prompt neutron emission, gives the post-neutron mass distribution; $M = 2E/v^2$. It is of interest to compare this post-neutron mass distribution with the radiochemical results. Also, since the point to point uncertainties in a kinetically determined mass distribution are smaller than in a radiochemical distribution, comparison of the post-neutron mass distribution from the present work with the pre-neutron mass distributions of double time-of-flight experiments is of interest and leads to new qualitative understanding of nuclear structure as related to the fission process.

To the knowledge of this author all previous time-of-flight experiments have been calibrated by the use of delay cables. This involves the determination of the time taken by a signal to pass through a given length of cable. The time-of-flight apparatus in this experiment was calibrated by means of heavy ions (^{127}I; ^{79}Br and ^{81}Br) accelerated to energies of 30 to 100 MeV by a tandem Van de Graaff accelerator. These artificial fission fragments are separated into groups of known velocities by an analyzer magnet and allowed to pass through the time-of-flight apparatus. This method of calibration, along with a velocity spectrum from the spontaneous fission of ^{252}Cf obtained at the same time, provides a universal calibration tool for time-of-flight experiments.

Finally, this work is being done as a preliminary step in the obtaining of three or four parameter correlation data. Many careful double time-of-flight and energy correlation experiments have been done. This two parameter experiment, in which an energy and a time-of-flight are correlated, brings together the techniques of measuring time and energy.

CHAPTER II

APPARATUS

The purpose of this experiment is the simultaneous measurement of the time-of-flight and the energy of a fission fragment. Briefly, this is accomplished by placing a source of fission fragments at one end of an evacuated flight tube. As a fragment leaves the source and starts down the tube it must pass through a very thin nickel foil, splashing out electrons. These electrons are detected and supply a $t = 0$ signal. At the far end of the flight tube of length, $D = 215.3$ cm, the fragment is detected with a solid-state detector. From this detector are taken both a fast timing signal which, along with the $t = 0$ signal, gives the time-of-flight of the particle, and a linear signal which is proportional to the energy of the particle. These signals are then recorded in a multichannel correlation analyzer as having occurred at the same time.

The apparatus used for these measurements is described in detail below.

I. MECHANICAL

Oak Ridge Research Reactor Facility

The time-of-flight apparatus at the neutron beam port, HB-1, of the Oak Ridge Research Reactor (ORR) has been described in detail in a previous work (Mruk, 1963).

Figure 1 is a schematic diagram of the time-of-flight apparatus. The zero-time detector chamber is a rectangular aluminum box and the

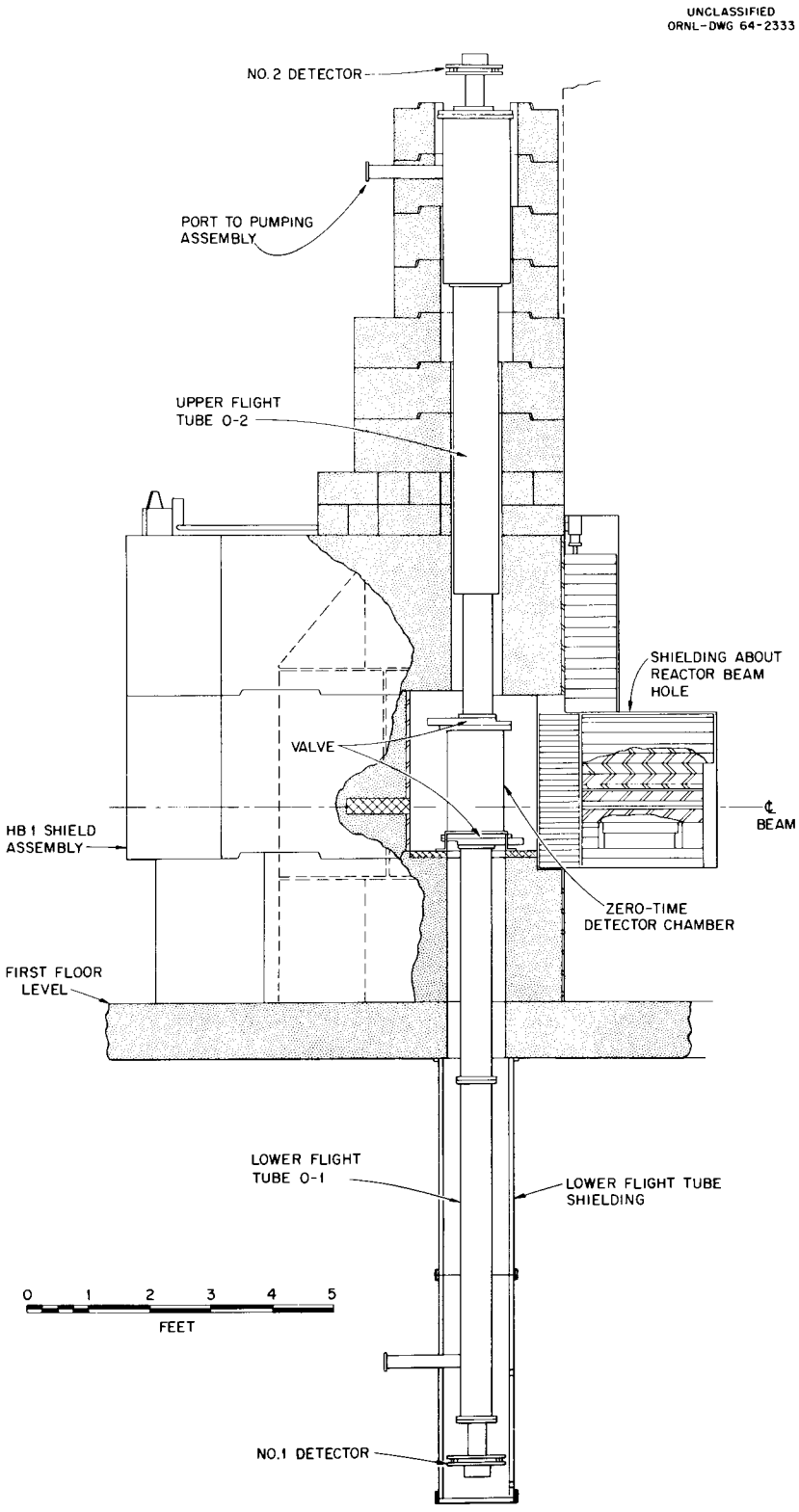

Figure 1. Schematic Diagram of ORR Time-of-Flight Apparatus.

flight tubes are aluminum cylinders. The overall length of the system is about six meters. For the present work only the upper flight tube was used. The nominal operating pressure was about 1×10^{-5} mm of Hg.

Figure 2 shows the zero-time detector chamber with the zero-detector in place. The detector itself will be described in detail later. However, it should be noted that the zero-detector is mounted on the cover plate of the zero box and is readily movable from one facility to another.

The neutrons available were pile neutrons that had passed through about 6 inches of beryllium. Activation measurements on gold and cobalt foils showed a neutron flux of about 2×10^{9} neutrons/cm^2sec below the cadmium cutoff and about the same above.

Tandem Van de Graaff Facility

The time-of-flight arrangement used at the tandem Van de Graaff accelerator is shown schematically in Figure 3. The zero box was constructed so as to accommodate the cover plate and zero-time detector used at the ORR facility. The flight tube was of aluminum and could be varied in length from about 2 meters to 3 meters.

The much smaller volume to be evacuated at the tandem facility made an elaborate vacuum system, such as the one at HB-1, unnecessary. One diffusion pump maintained an operating pressure of about 7×10^{-6} mm of Hg.

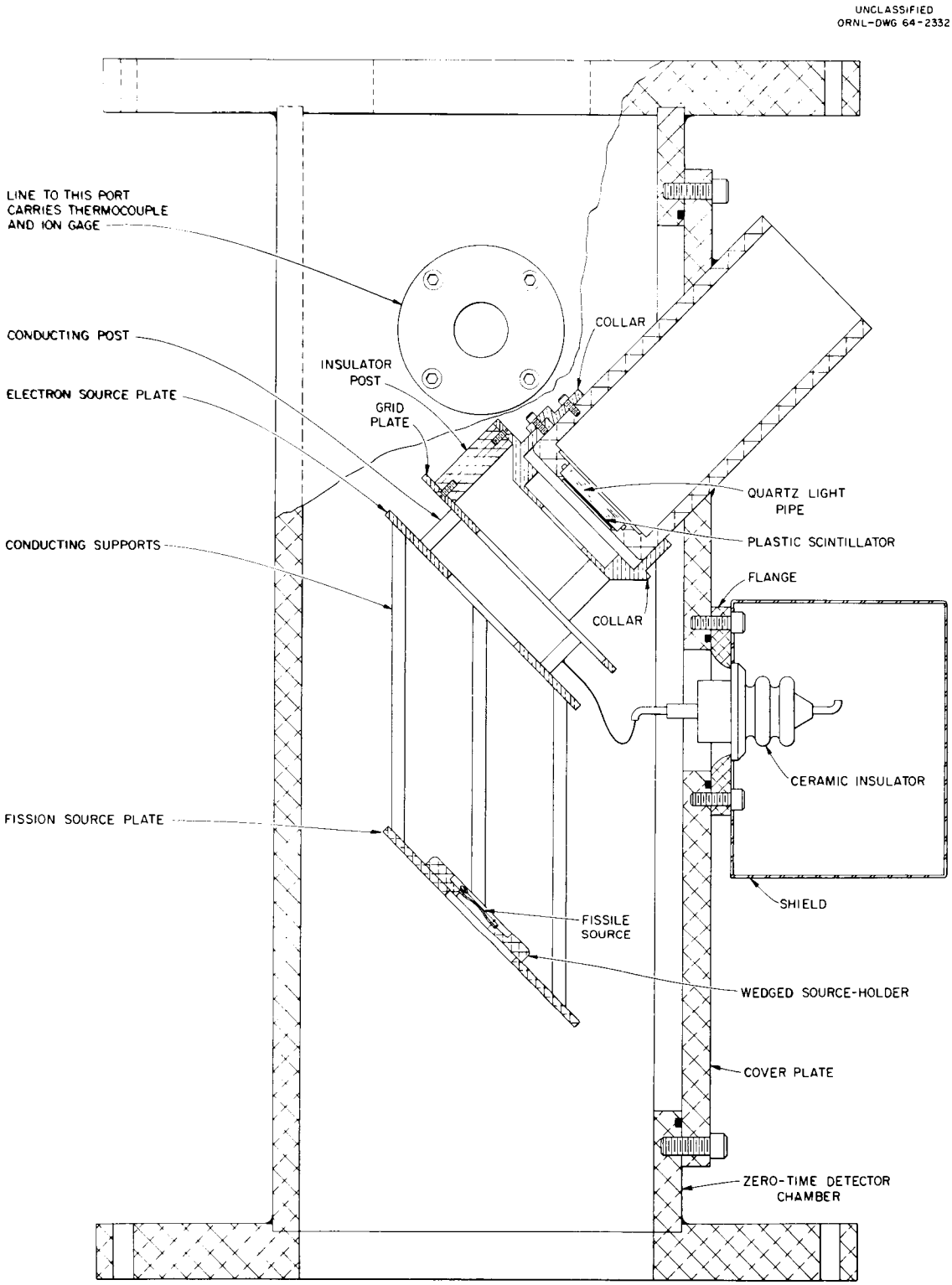

Figure 2. Zero Time Detector.

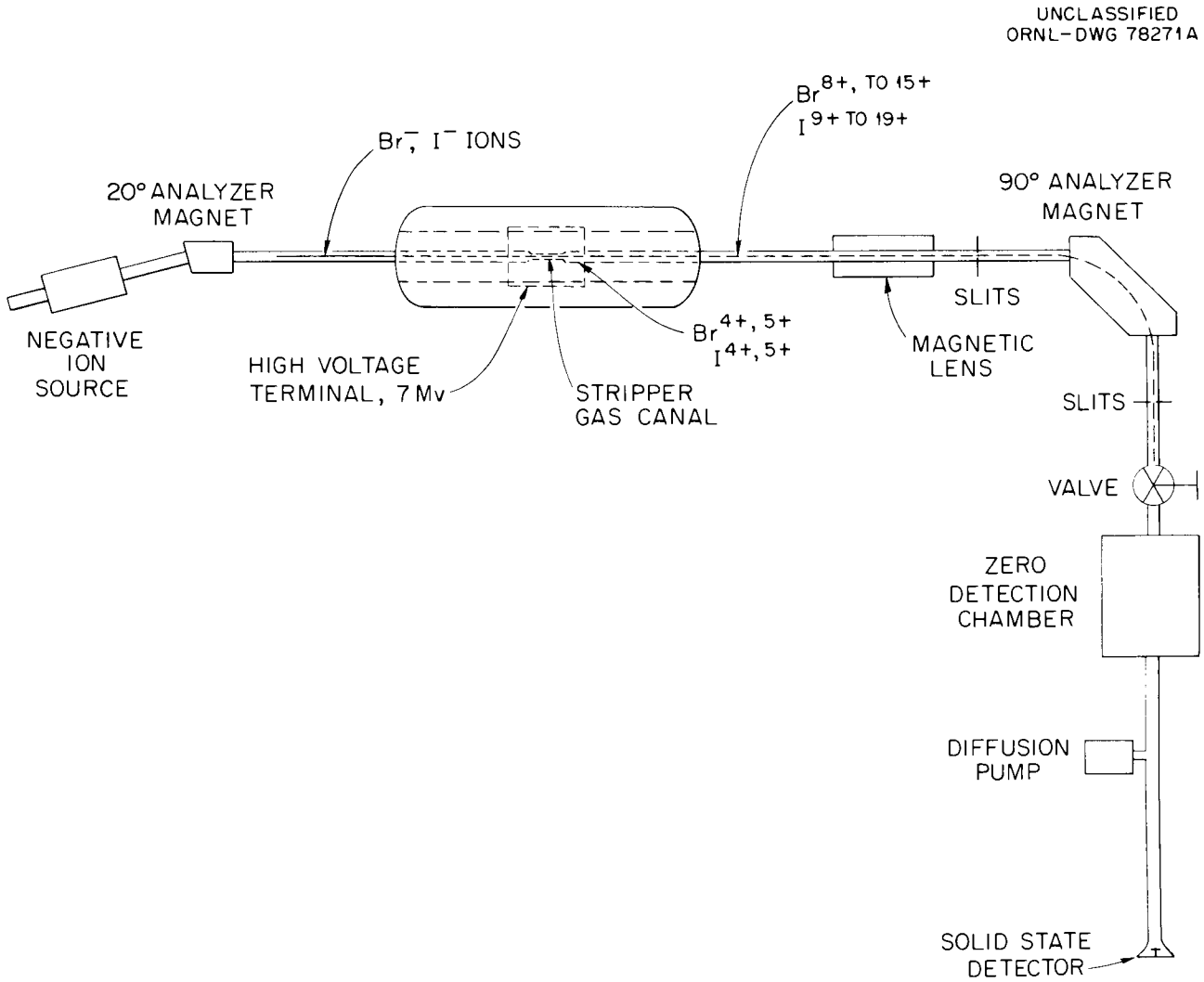

Figure 3. Experimental Arrangement for Energy and Time-of-Flight Measurements on Heavy Ions from the Tandem Van de Graaff Accelerator.

II. ELECTRONICS

System Design

Figure 4 is a block diagram of the energy-time system. It shows how four parameters, i.e., the energies and times-of-flight of both fission fragments, may be correlated. In the present work only one side of the system was used.

The energy (linear) signal and the timing (fast) signal are taken from the same remote detector by means of a fast-response transformer coupling scheme (Williams and Biggerstaff, 1964). The current pulse from a silicon surface barrier detector passes through the transformer primary to a low-noise charge sensitive pre-amplifier, as shown in Figure 5. The timing signal, taken from the transformer secondary, is amplified by a fast amplifier, the output of which triggers a remotely-controlled tunnel diode discriminator. The transformer coupling scheme insures that no charge can be transferred to or from the energy analysis system and that noise voltage generated by the fast amplifier will be divided between the detector and the charge sensitive amplifier input in inverse proportion to their respective capacitances.

The fast amplifier (Williams and Neiler, 1962) is voltage sensitive, has a voltage gain of $\sim$250 and a rise time of 3.5 nsec (1 nsec = 10^{-9} sec). The fast amplifier output drives a tunnel diode discriminator which provides the "start" signal for the time-to-pulse-height converter (TPHC).

As is shown in Figure 4, a time delay longer than the longest fragment flight time is used in the time-zero signal line and the zero signal is used as a "stop" signal for the TPHC.

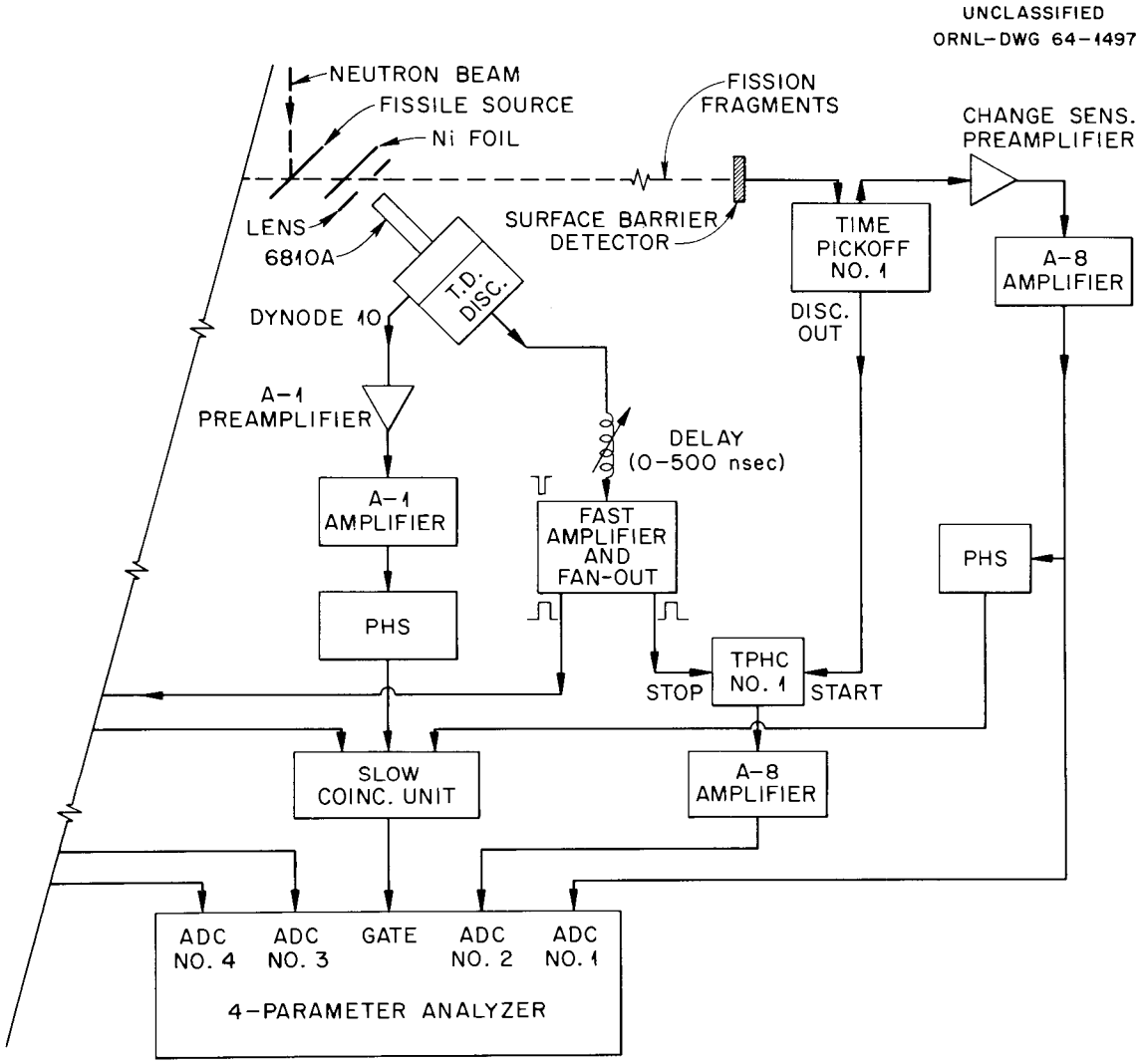

Figure 4. Block Diagram of Energy, Time Correlation System.

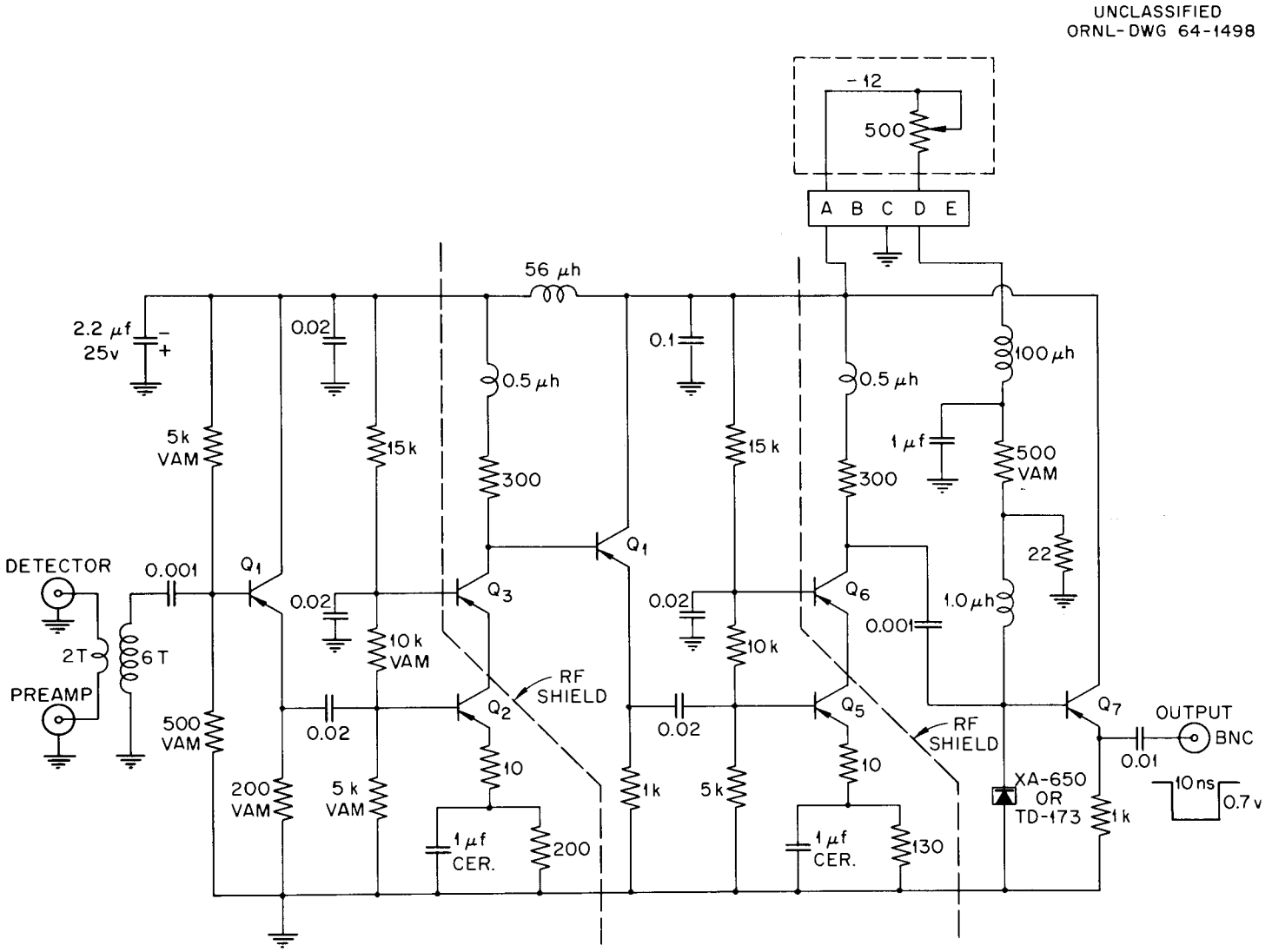

Figure 5. Time-Pickoff Unit.

The zero detector (Figure 2) consists of a thin nickel foil ($\sim$70 $\mu g/cm^2$) through which the particle of interest must pass. About 70 electrons are splashed from the foil and focused electrostatically onto a 1 1/2 inch diameter, thin plastic (NE 102)* scintillator attached to a 1/4 inch thick quartz light pipe. Optically coupled to the light pipe is an RCA 6810A photomultiplier tube. The current signal from the anode of the phototube is fed directly to a remotely controlled, tunnel diode discriminator. The output from this discriminator is delayed, amplified and used as the "stop" signal for the TPHC.

The outputs from the TPHC and the charge sensitive linear preamplifier are further amplified by standard A-8 double-delay-line amplifiers and then recorded on punched paper tape by a 256 x 256 correlation pulse-height analyzer. On-line monitoring of the events recorded in each parameter was accomplished by means of a conventional magnetic core analyzer (Nuclear Data, Model 130, 512 channel analyzer).

System Performance

Noise. In order to determine the noise contribution of the time pick-off unit to the energy resolution of the system, americium and curium alpha particle spectra were obtained with a 50 mm^2 surface barrier detector operated on the pulse-height vs. bias plateau (Figure 6). A resolution of 17 keV, full width at half maximum, (FWHM), was obtained with and without the time pick-off unit in the circuit. A comparison of the widths of the pulser peaks shows an increase of $\sim$2 keV when the

*Purchased from Nuclear Enterprises, Ltd., Winnepeg, Manitoba.

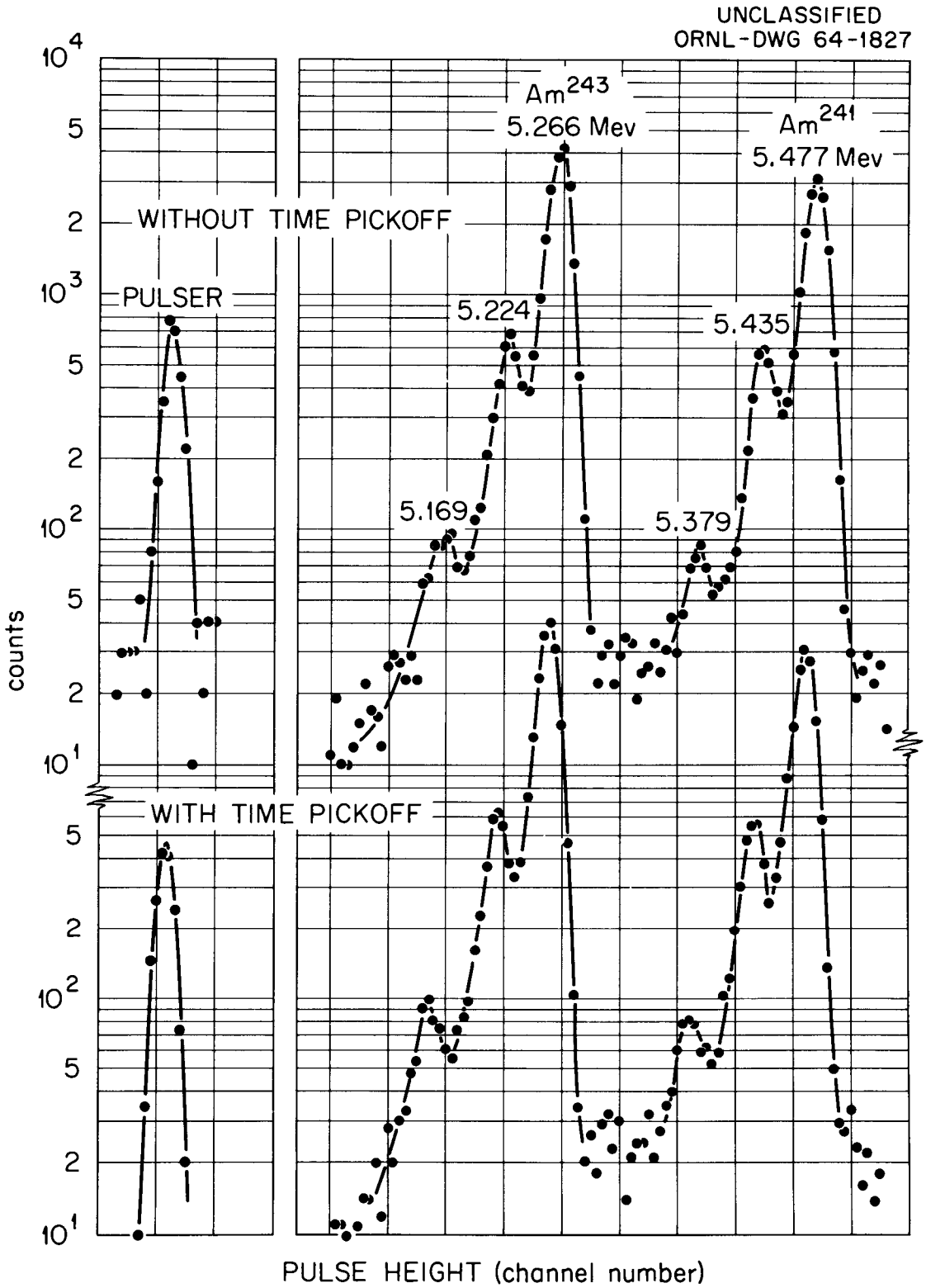

Figure 6. Comparison of Alpha Particle Pulse-Height Spectra with and without Time-Pickoff Unit.

time pick-off unit is introduced. The same test was performed on detectors of large area (450 mm^2) and again no change in alpha particle line width was observed.

Heavy ion measurements. High energy (30-100 MeV) bromine and iodine ions (specifically, ^{79}Br and ^{81}Br; or ^{127}I) were obtained from the tandem Van de Graaff accelerator. These ions were magnetically analyzed in a 90° deflecting magnet, thus yielding particles of constant ME/q^2, where M, E, and q are the ion mass, energy, and charge, respectively. Since q is an integral number of electron charges, discrete energy groups are obtained for ions of a given mass. (Heavy ion measurements will be discussed in greater detail in the next chapter.) After acceleration and magnetic analysis the ions passed through a nickel foil of $\approx$70 $\mu gm/cm^2$ thickness, splashing out electrons and supplying a time-zero signal. The ions were then incident on a surface barrier detector placed two or three meters away, supplying a signal linearly related to the particle energy and a fast timing signal. The electronic system shown in Figure 4 was used to obtain time spectra, pulse-height (energy) spectra, and energy, time correlation data (which will be discussed presently). A typical time spectrum for ^{127}I is shown in Figure 7; for $^{79,81}Br$ in Figure 8. Typical energy spectra are shown in Figures 9 and 10.

The time resolution (FWHM) as a function of particle energy and of particle velocity is shown in Figures 11 and 12. In the region of interest the time resolution varies from about 1.4 to 2.5 nsec. It is apparent from Figure 11 that the time resolution of the system is regularly related to particle energy only for particles of a given mass.

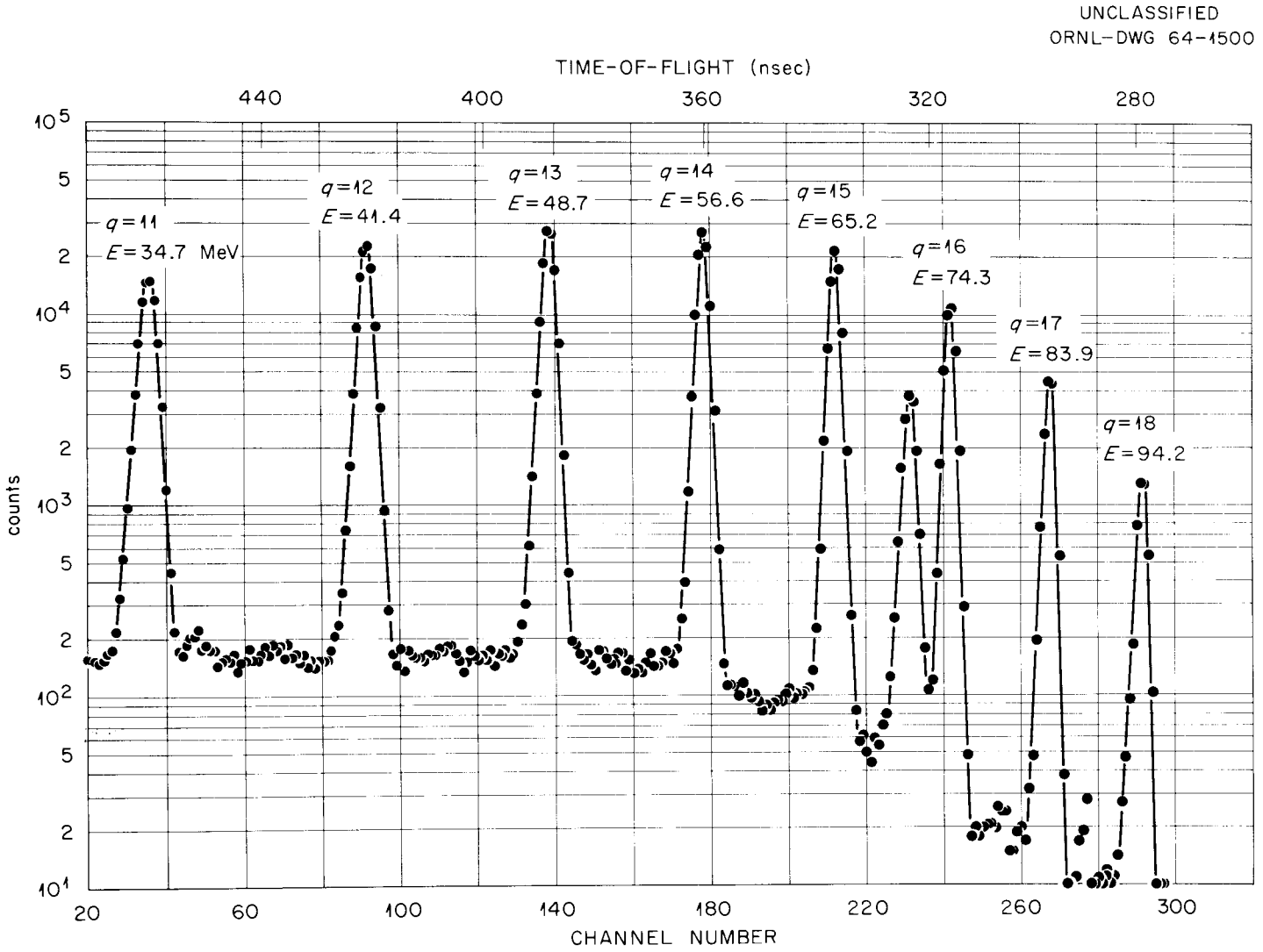

Figure 7. Time-of-Flight Spectrum for ^{127}I Ions.

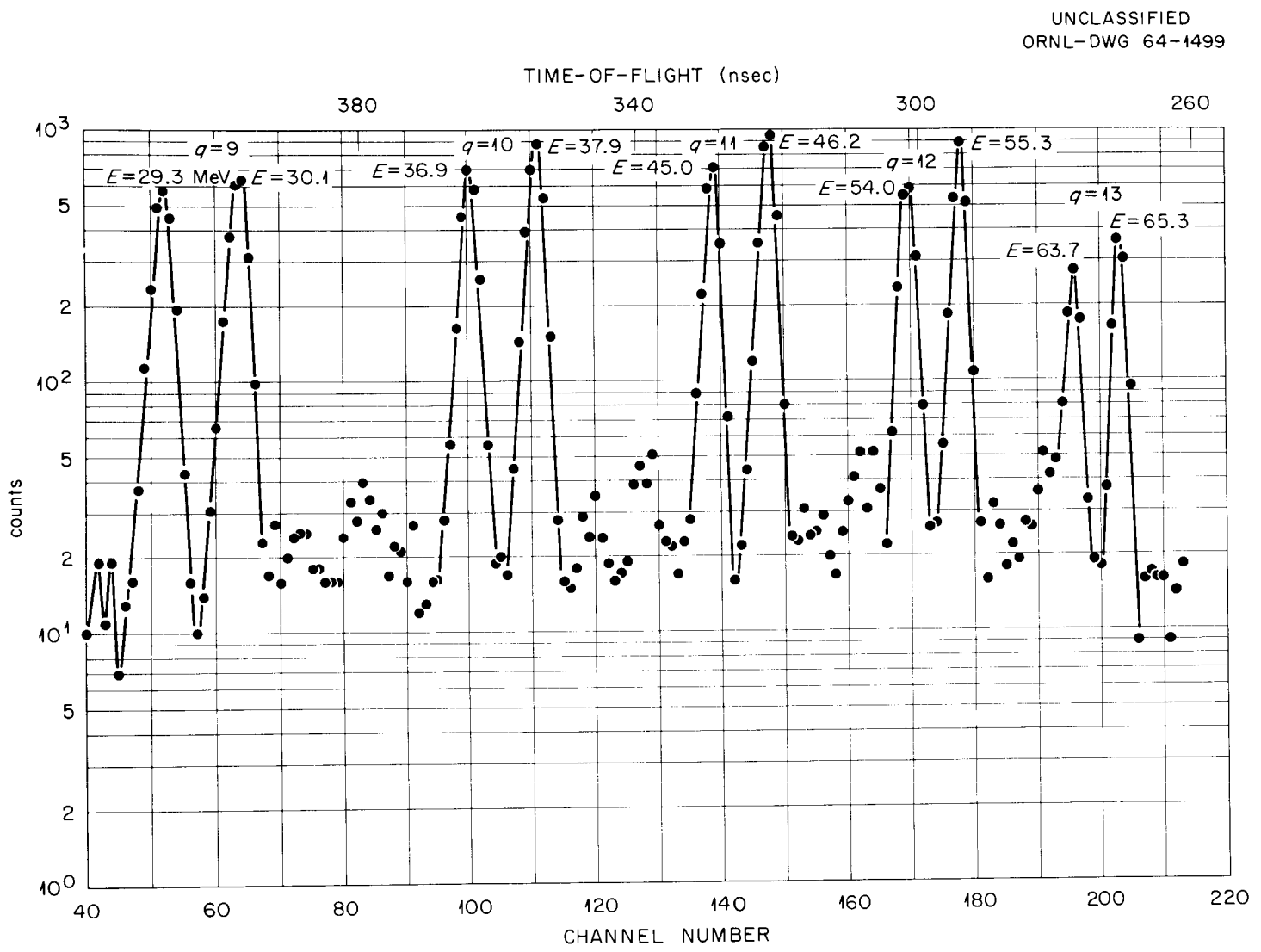

Figure 8. Time-of-Flight Spectrum for ^{79}Br and ^{81}Br Ions.

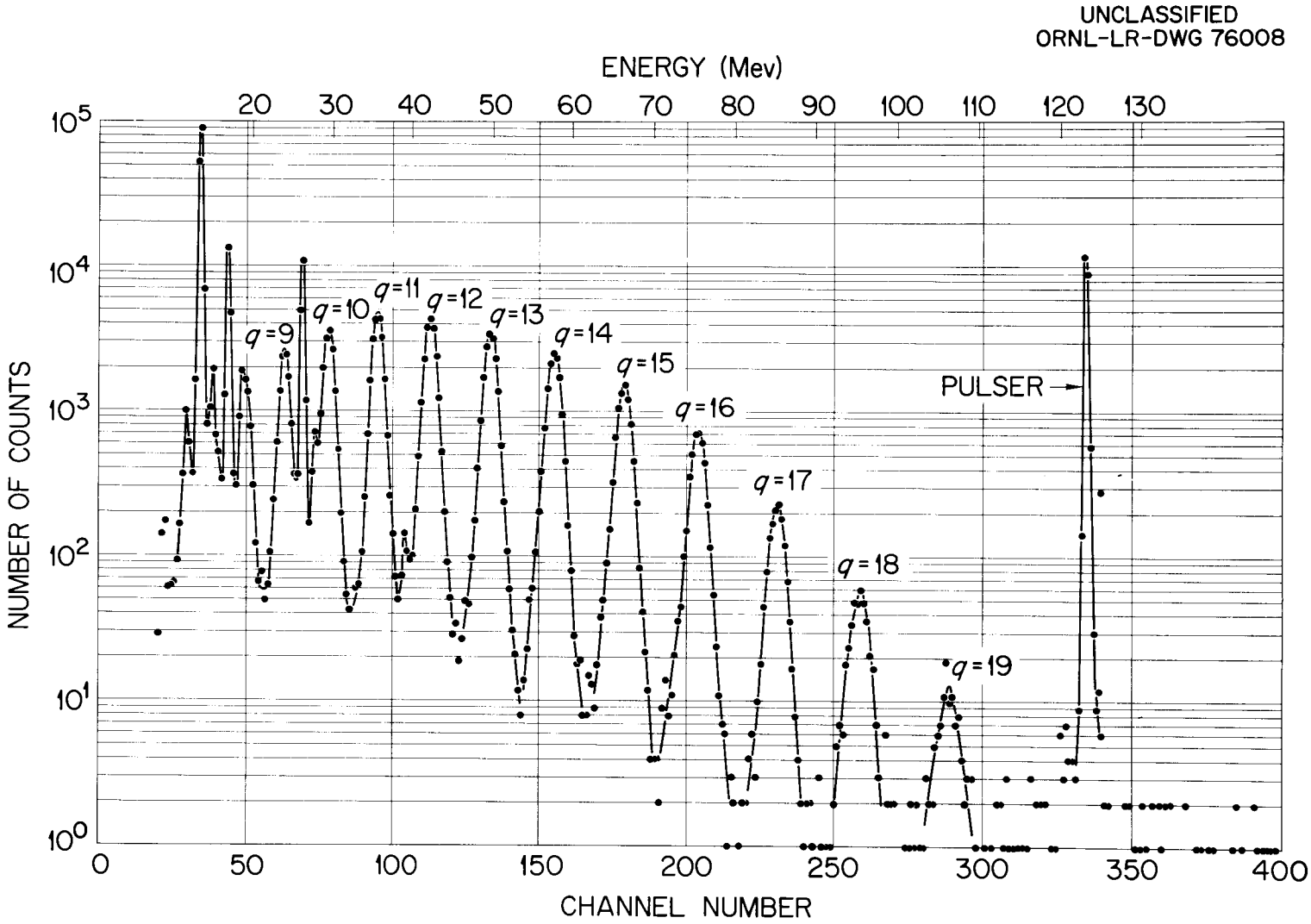

Figure 9. Pulse-Height (Energy) Spectrum for ^{127}I Ions.

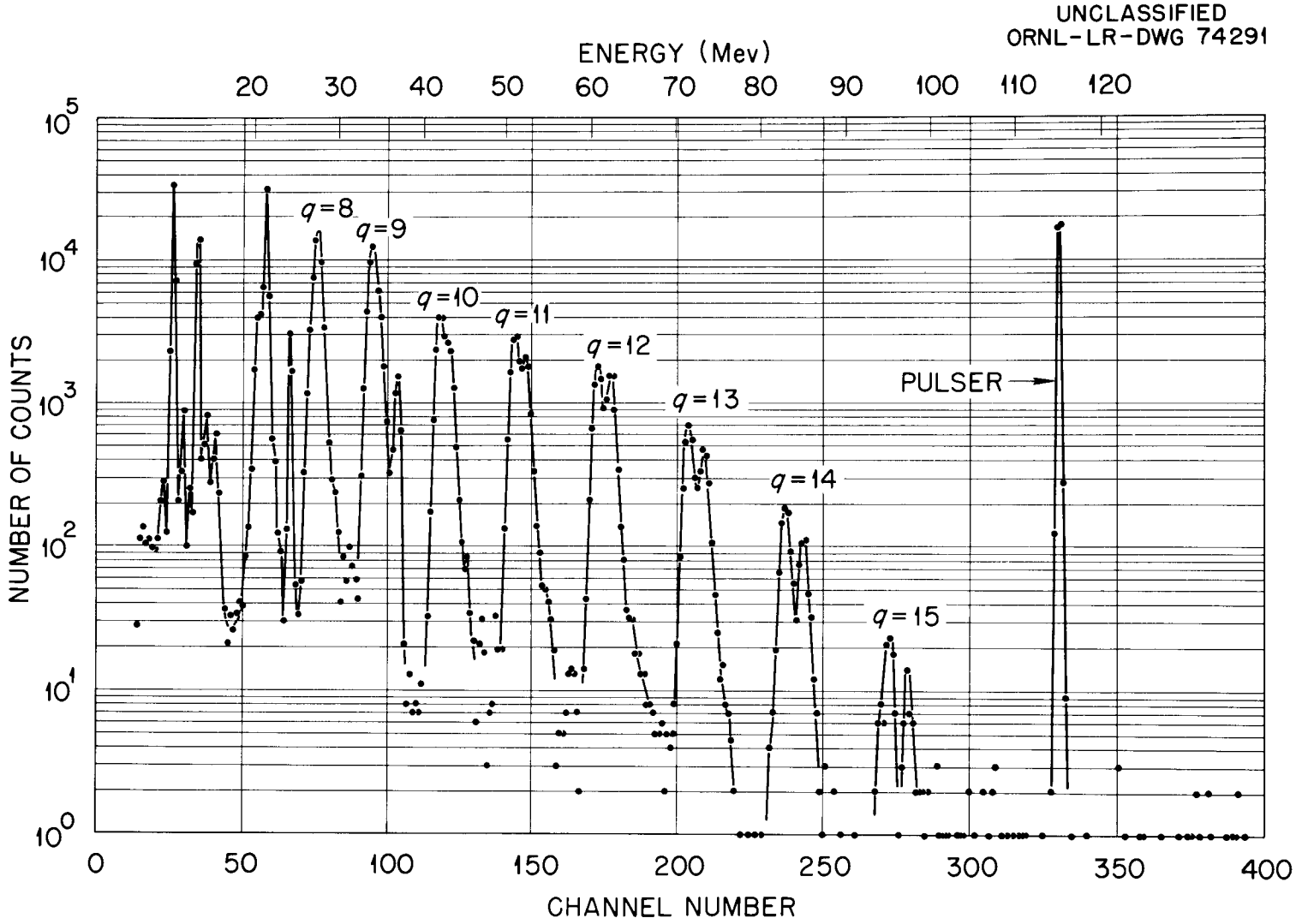

Figure 10. Pulse-Height (Energy) Spectrum for ^{79}Br and ^{81}Br Ions.

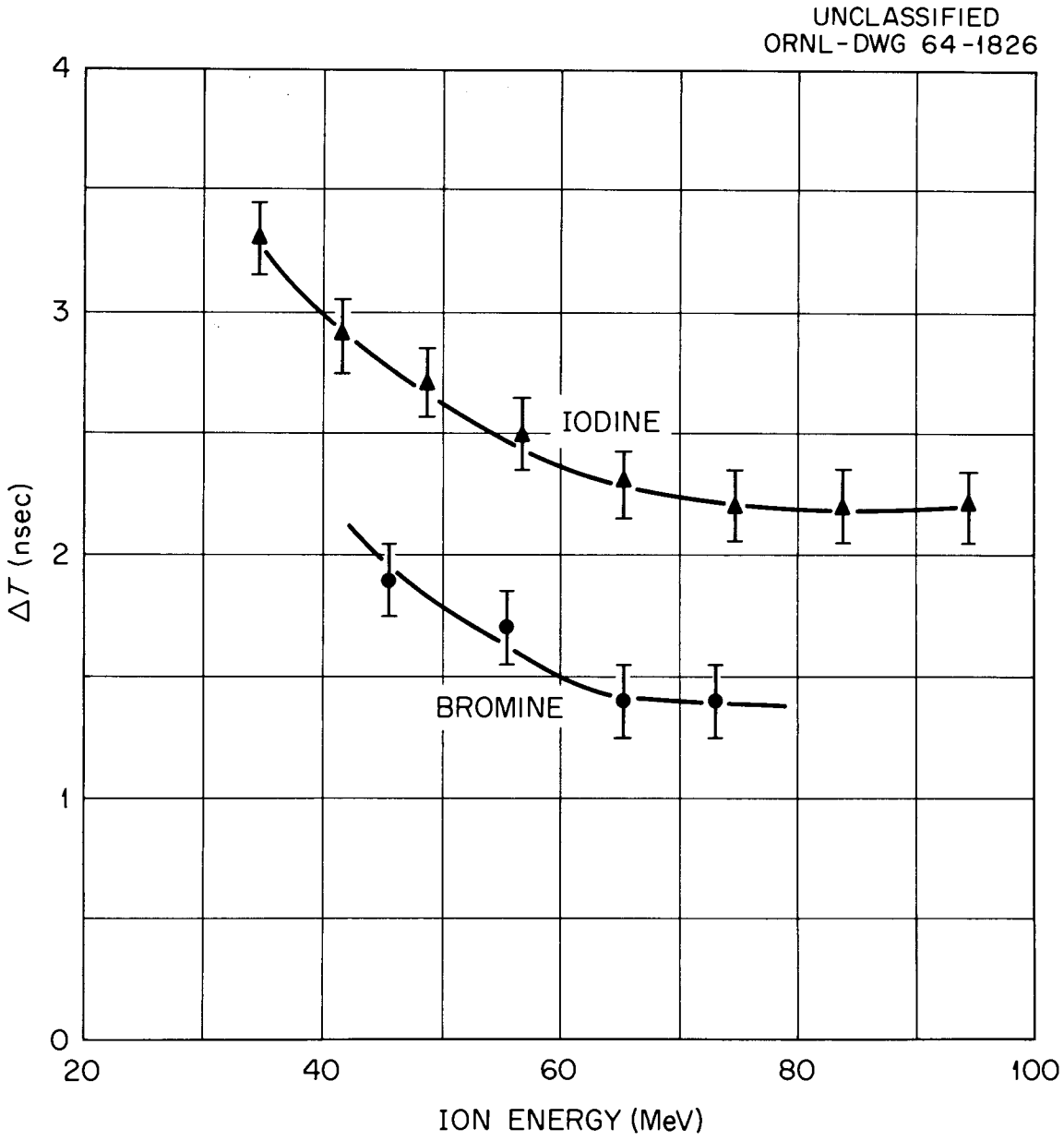

Figure 11. Time Resolution as a Function of Particle Energy.

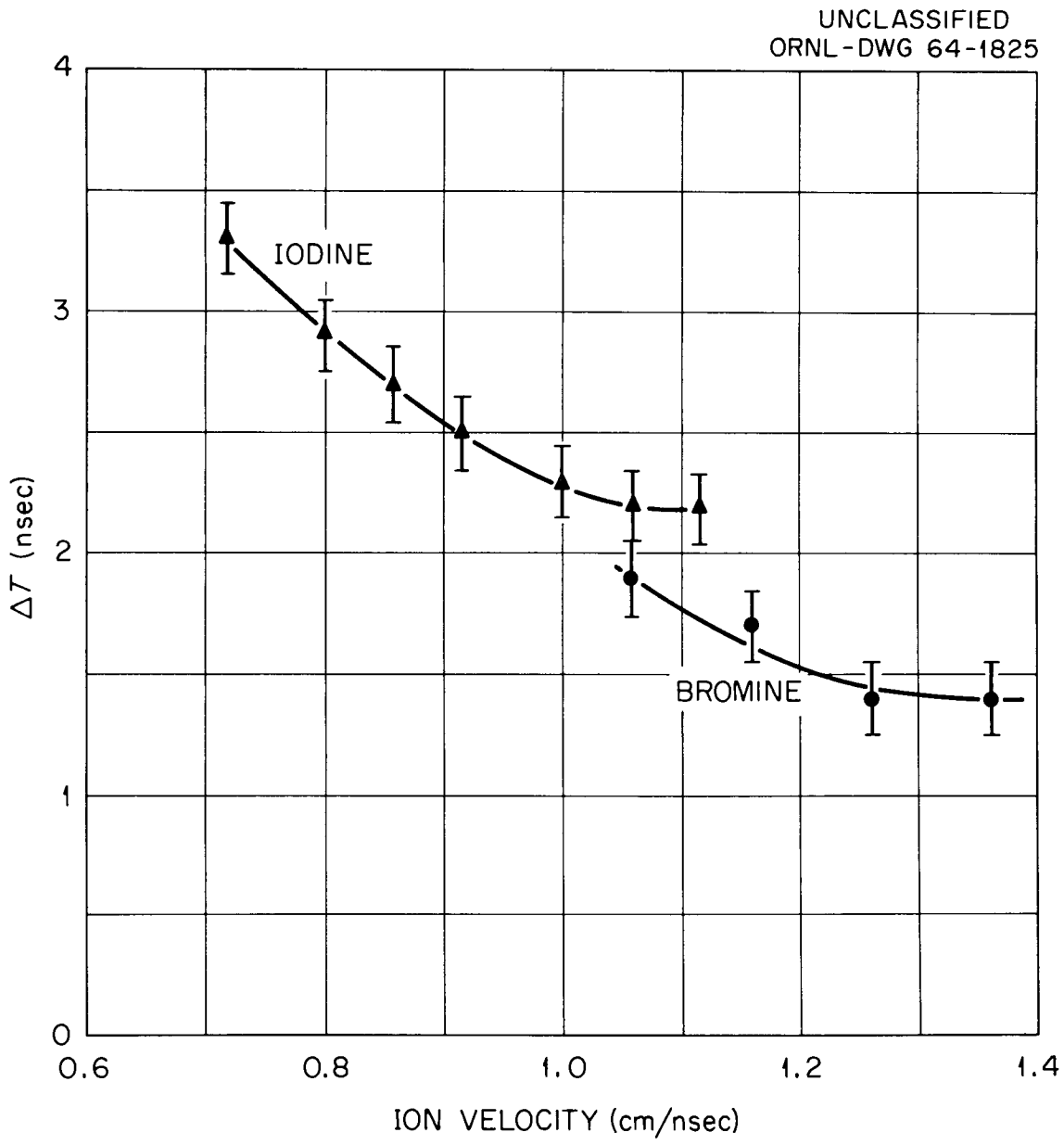

Figure 12. Time Resolution as a Function of Particle Velocity.

However, the curves of Figure 12 show that the time resolution might well be a monotonically decreasing function of particle velocity.

A possible explanation for this behavior may be in the kinetics of the electrons that are splashed from the nickel foil in the zero detector. Measurements of the signal amplitude from the zero detector in correlation with fission fragment energies and velocities, described in Appendix B, indicate that the zero detector signal amplitude is independent of fragment energy and velocity. This is rather strong evidence that each fission fragment produced about the same number of electrons. However, it does not seem unreasonable to assume that the electrons produced by the fragments of greater velocity would have a slightly greater component of velocity in the direction of the electron detector. In addition, these electrons would be produced in a shorter time, since the faster fragments would remain in the vicinity of the foil surface for a shorter time than would the slower fragments. Thus, the faster fragments would probably produce electrons that were slightly more bunched than those produced by slower fragments. The results of these two effects would be that the zero signals produced by the fission fragments of greater velocity would have a slightly faster rise time than those of the slower fragments, and there would be a slightly smaller spread in rise times for the faster particles. If the above arguments are valid, then one would expect better time resolution for the faster particles.

Energy measurements on heavy ions from a tandem Van de Graaff accelerator have been reported (Schmitt, Walter, Neiler, Moak, Gibson, and Thomas, 1963) and will be discussed in some detail in the next

chapter. Suffice it to say here that the energy resolution was found to be about 1.5 MeV (FWHM) and appears to be inherent in the detectors.

Energy, time correlation measurements on heavy ions. In order to measure the mass resolution of the system, correlated energy and time-of-flight measurements were made on the heavy ions from the tandem Van de Graaff. Contour plots for iodine and bromine are shown in Figures 13 and 14, respectively. Constant mass lines for M = 124, 127, and 130, and M = 77, 79, 81, and 83 are shown.

Having measured the energies and times-of-flight of several energy groups of these heavy ions, one is able, through the relation $E = Mv^2/2$ (relativistic effects are less than 0.2 per cent), and through appropriate transformations of the data, to obtain mass distributions. These should, of course, peak about the masses, 126.9 and 78.9, 80.9, as shown in Figure 15. The mass resolution (FWHM) is about 3.2 amu for iodine and 1.8 amu for bromine, or about 2.5 per cent.

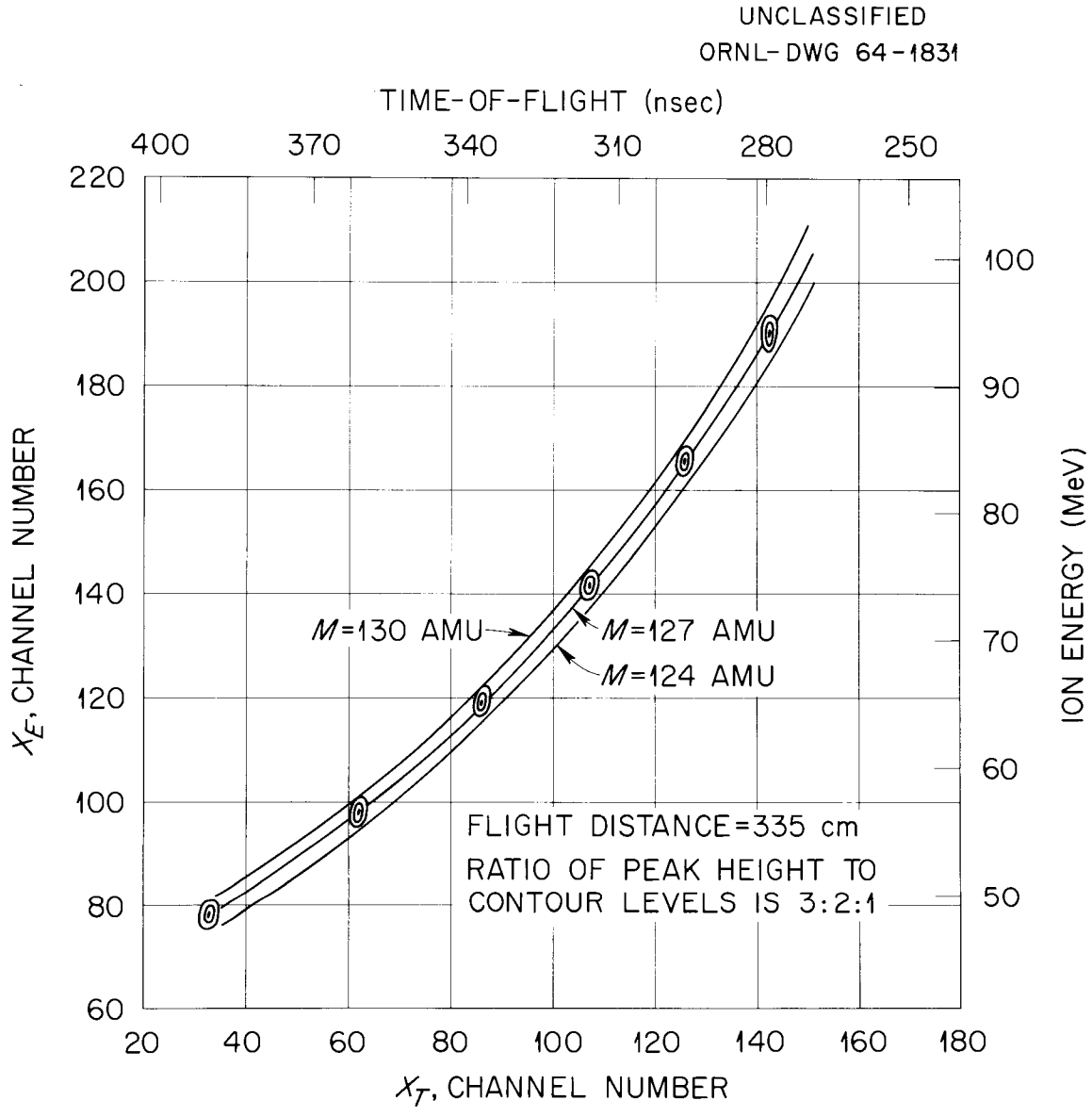

Figure 13. Energy, Time Correlation Data for ^{127}I Ions.

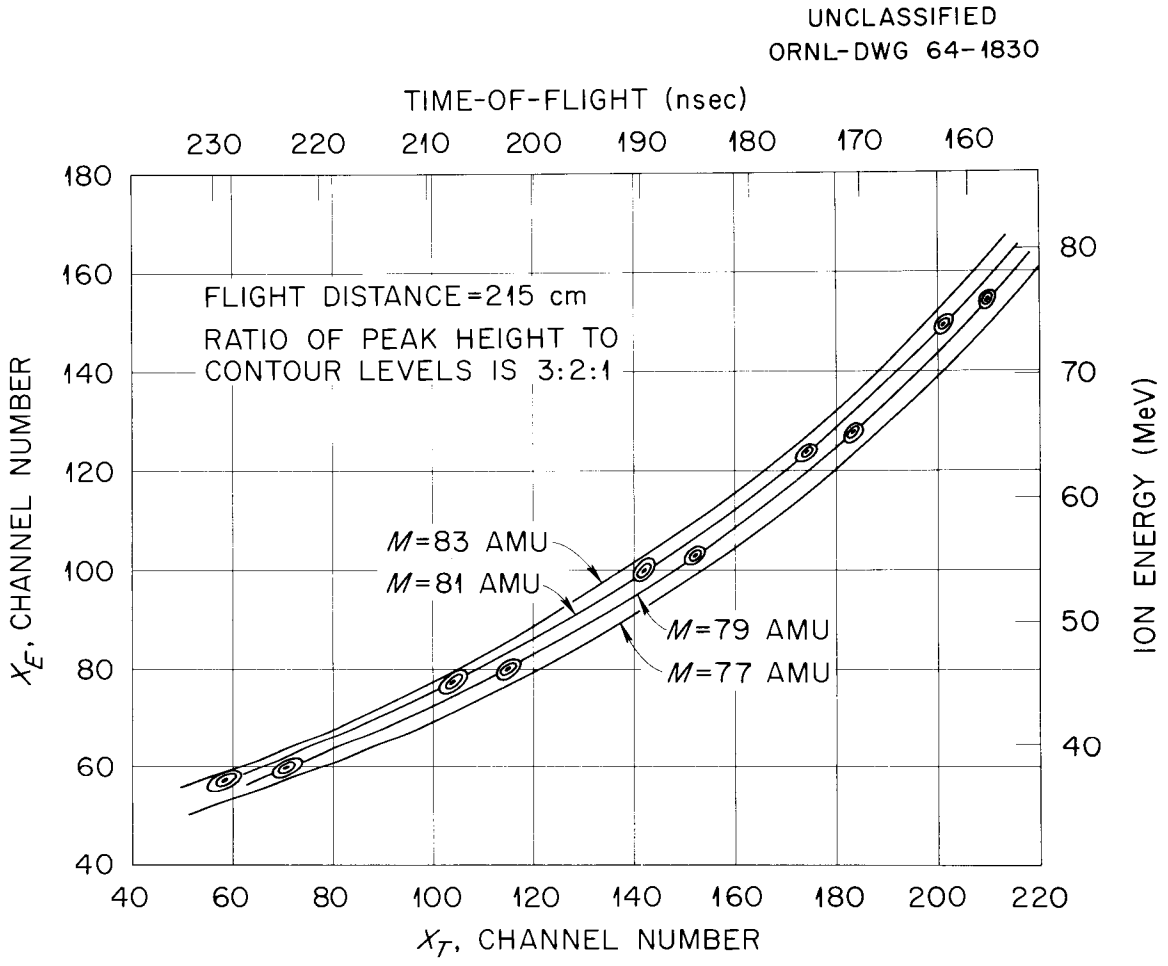

Figure 14. Energy, Time Correlation Data for ^{79}Br and ^{81}Br Ions.

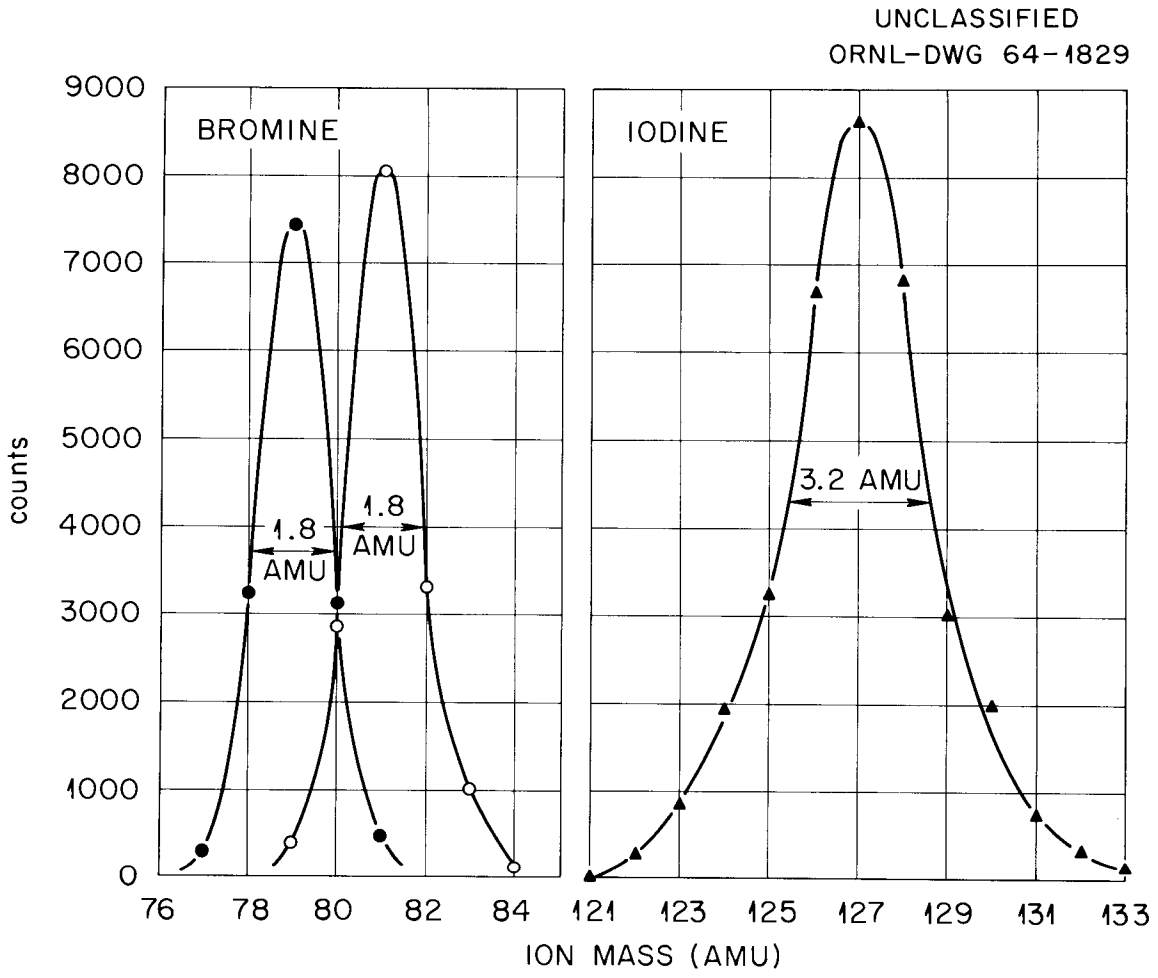

Figure 15. Mass Distributions from Bromine and Iodine Ion Energy, Time Correlation Experiments.

CHAPTER III

SYSTEM CALIBRATION

A detailed account of the methods and procedures for obtaining ^{127}I and $^{79,81}Br$ ions in the energy range 30-120 MeV is given by Moak, et al (Maok, Neiler, Schmitt, Walter and Wells, 1963) and in Appendix A. The method for obtaining groups of ions of constant E/q^2 and V/q by magnetic analysis is described, along with the procedure for identifying the charge states of the various groups. Therefore, this chapter will begin on the premise that there are available groups of ions (^{127}I and $^{79,81}Br$) of various energies and velocities, and that these energies and velocities are known.

I. ENERGY CALIBRATION

Evidence for Mass Dependence of the Pulse-Height vs. Energy Relationship in Solid-State Detectors

When charged particles of constant mass strike a solid-state detector, the resulting output pulse-heights are linearly related to the energies of the particles. There is strong evidence, however, that the pulse-height also depends on the mass of the incident particle. Figure 16 shows energy vs. pulse-height curves obtained with $^{79,81}Br$ and ^{127}I ions from the tandem Van de Graaff accelerator. An alpha particle curve has been added for reference. The bromine and alpha curves are parallel while the iodine curve has a slightly greater slope. There is some slight difference between these curves and those reported by Schmitt, et al (Schmitt, Walter, Neiler, Moak, Gibson and

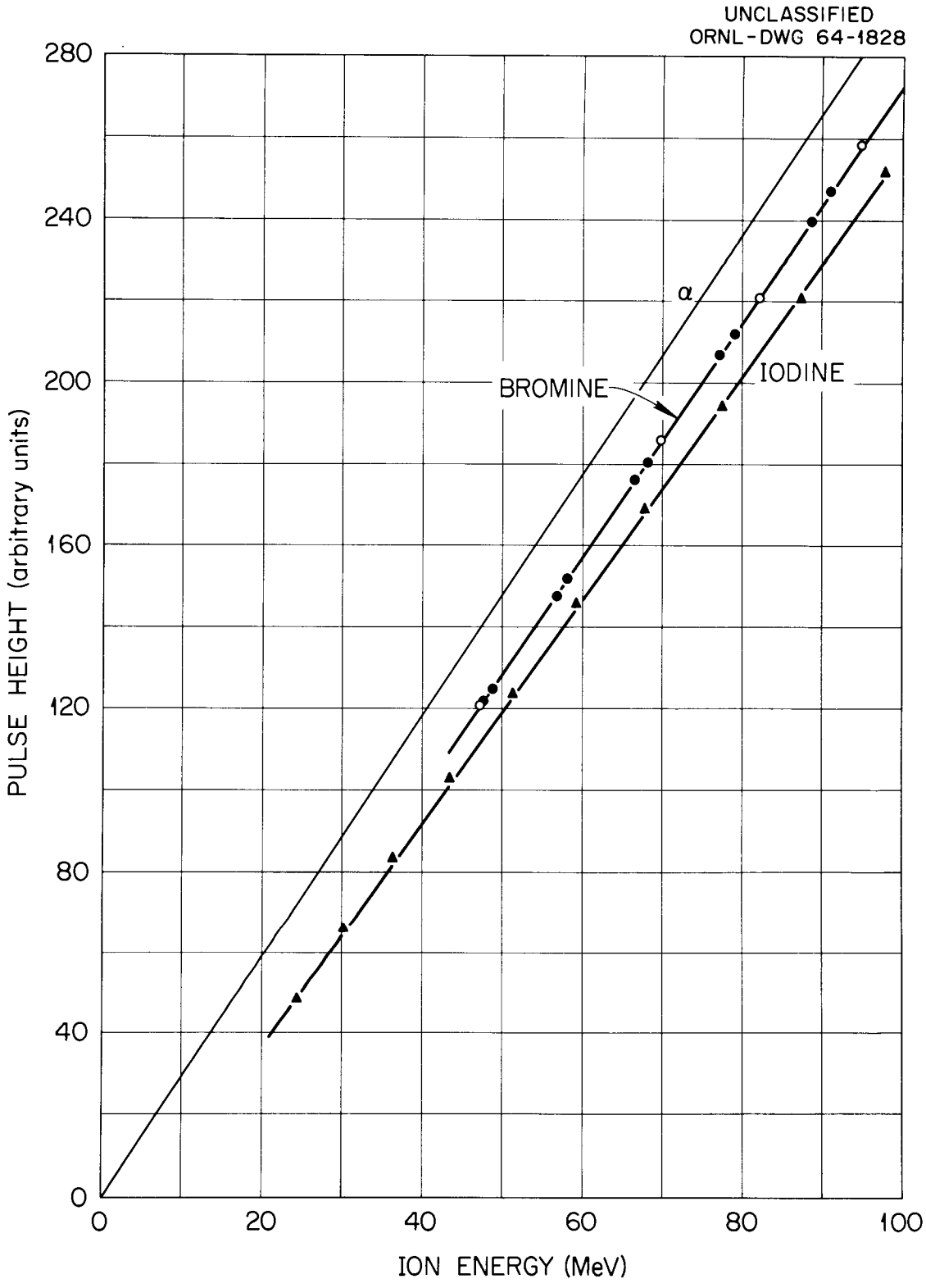

Figure 16. Pulse-Height vs. Energy Relation for Solid-State Detector.

Thomas, 1963) in that their bromine line lay slightly closer to the alpha line than to the iodine line. This could well be due to slight differences in the detectors used and is probably of no consequence.

The two different sets of points in the bromine curve are from runs at different magnet frequencies. The excellent straight line defined by these points is an indication of the precision of the magnet calibration and of the charge independence of the energy, pulse-height relation.

Energy vs. Pulse-Height

The sharp energy peaks such as shown in Figures 9 and 10 associate an energy with the pulse-height analyzer channel at the centroid of each peak. Thus, one obtains energy vs. channel number relationships for each run. A stable mercury-relay pulser with variable amplitude output is capacitively coupled to the charge sensitive pre-amplifier as shown in Figure 17. In this way reproducible pulser points are included in each run. This relationship of pulser setting (or pulse-height) vs. channel number associates a pulse-height with each of the energy peaks and yields the pulse-height vs. energy relations shown in Figure 16.

Calibration Scheme

Figure 16 shows that for a given mass and in the energy range of interest, the energy vs. pulse-height relation is linear. Therefore, one should be able to write the relations as: $E = a(M)X_e + b(M)$, where X is the energy channel number. This, of course, assumes good integral linearity for the pulse-height analyzer. The functions a(M)

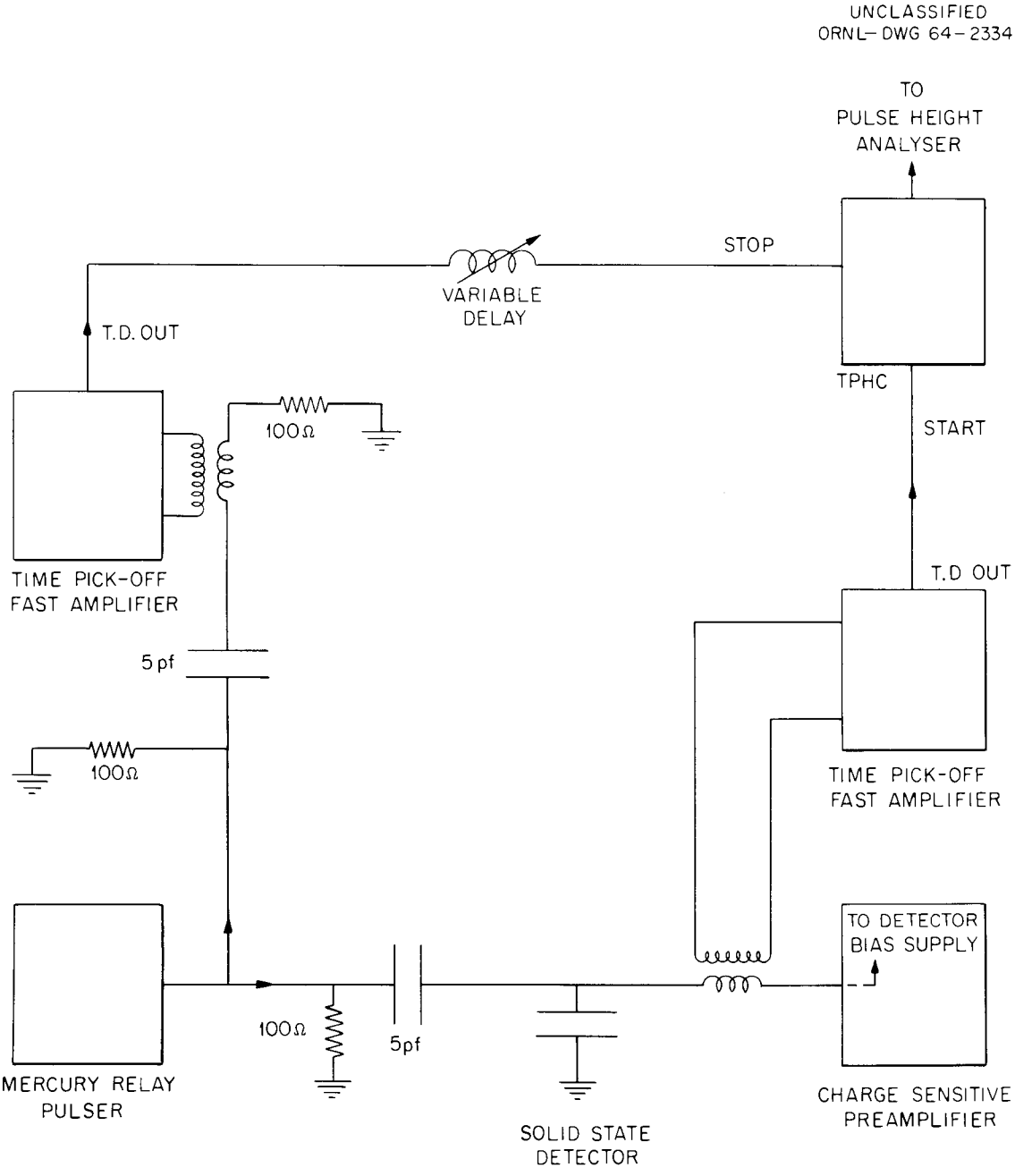

Figure 17. Method for Coupling Mercury-Relay Pulser into Time-of-Flight Energy System.

and b(M) are unknown. However, recent work (Schmitt, Neiler, Walter, Gibson, and Thomas, 1964) shows that a(M) and b(M) may be quite linear over the range of fission fragment masses. With this assumption, the calibration equation then becomes: $E = (a_1 + a_2M)X_e + b_1 + b_2M$. The constants a_1, a_2, b_1, and b_2 for a given run were determined as follows: from the pulser (PH) vs. channel number (X_e) curve of the run, two pulser points, PH_1 and PH_2, were chosen. These are, of course, associated with X_e^1 and X_e^2. Then, from the energy vs. PH curves for bromine and iodine, PH_1 is associated with E_1^I and E_1^{Br}; PH_2 is associated with E_2^I and E_2^{Br}. Now one may write:

$$E_1^I = (a_1 + 126.9\ a_2)X_e^1 + b_1 + 126.9\ b_2,$$

$$E_1^{Br} = (a_1 + 79.9\ a_2)X_e^1 + b_1 + 79.9\ b_2,$$

$$E_2^I = (a_1 + 126.9\ a_2)X_e^2 + b_1 + 126.9\ b_2,$$

$$E_2^{Br} = (a_1 + 79.9\ a_2)X_e^2 + b_1 + 79.9\ b_2.$$

Solving these four equations simultaneously for the constants gives the desired calibration.

Universal Calibration Scheme for Solid-State Detectors

For the calibration method described above to be useful to an experimenter using semiconductor detectors he must have available heavy ions of known energy in the energy range of interest; or he must be able to relate the pulse-heights from his pulser to the energy, pulse-height relations determined by others. It is suggested that this relation may be determined by the use of the fission fragments from the spontaneous fission of ^{252}Cf.

A post-neutron ^{252}Cf pulse-height spectrum from a semiconductor detector, such as shown in the lower half of Figure 18 may be used as an energy calibration tool for that detector, as is illustrated by Figure 18. The energy vs. pulse-height relation for solid-state detectors has been determined for masses 80 and 127 by the measurements on ^{127}I and $^{79,81}Br$ ions previously described. The ^{252}Cf pulse-height spectrum fixes two points that are always reproducible for a given detector simply by recording a ^{252}Cf pulse-height spectrum. This obviously assumes that the ^{252}Cf fission fragments are not degraded in energy before reaching the detector. We have chosen to define these two points as the point in each peak midway between the 3/4-maximum points, as is shown in Figure 18. Then, for masses 80 and 127, the following energies may be associated with these two points: for the light fragment, $E_{L,127} = 107.01$ and $E_{L,80} = 100.57$ MeV; for the heavy fragment, $E_{H,127} = 78.45$ and $E_{H,80} = 73.69$. With the previously discussed assumption that the energy calibration is linearly dependent on mass, the calibration equation may be written as

$$E = (a_1 + a_2 M)X + b_1 + b_2 M , \qquad (1)$$

where X = pulse-height; or channel number, if the integral linearity of the pulse-height analyzer is good. With the two values of X defined by the points in the ^{252}Cf spectrum and two values of mass and energy known for each point, equation (1) gives four equations which may be solved for a_1, a_2, b_1, and b_2. This is the desired calibration. It should be pointed out that the values of $E_{L,127}$, $E_{L,80}$, $E_{H,127}$, and $E_{H,80}$ quoted above were not obtained directly from the curves of Figure 18, but were obtained by averaging the results of three such

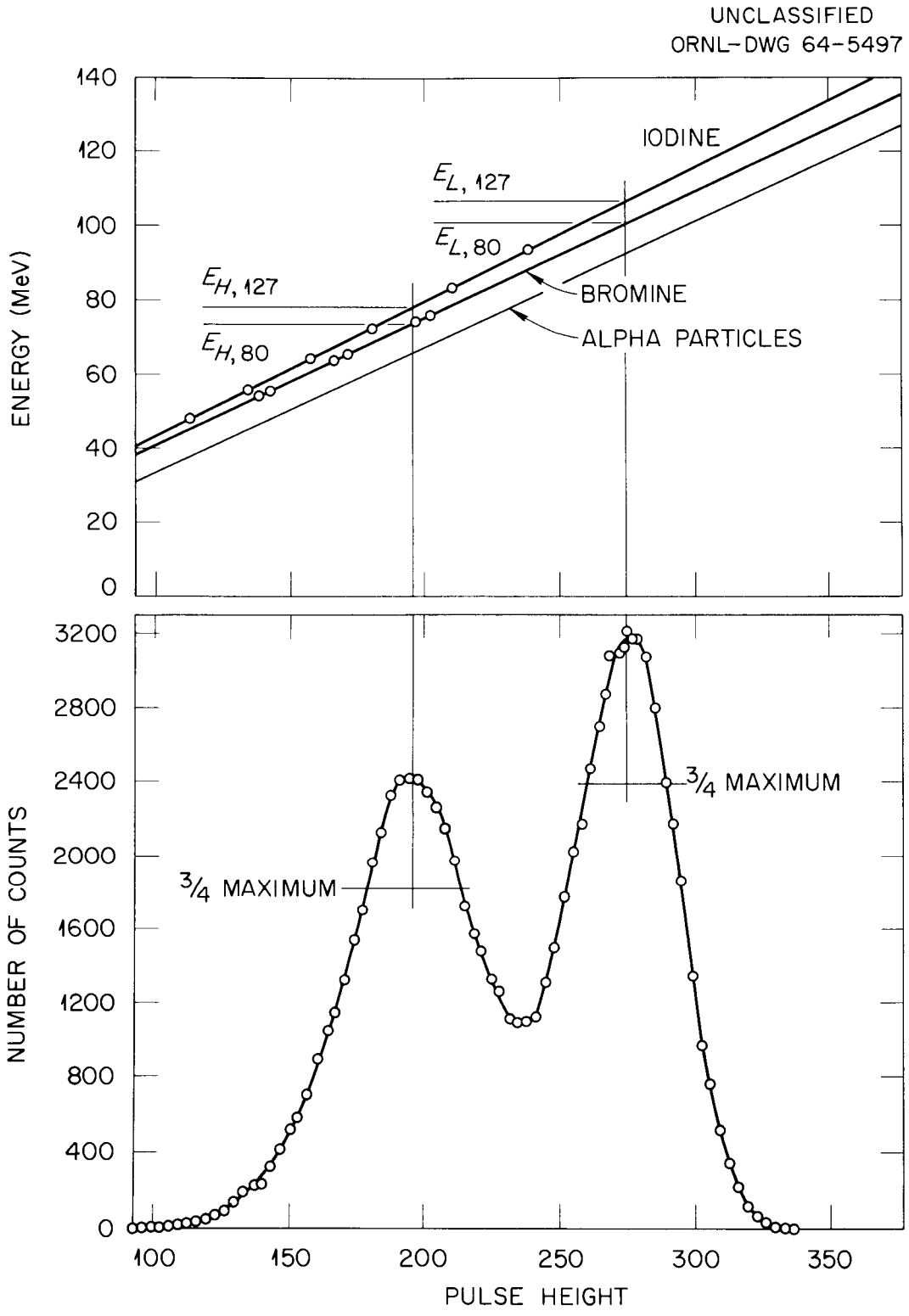

Figure 18. Absolute Energy Calibration of Solid-State Detectors for Fission Fragments.

experiments. Variations in the corresponding energies were ± 0.2 MeV or less.

II. TIME CALIBRATION

The time-of-flight system was calibrated by measuring pulse-heights corresponding to the times-of-flight of heavy ions ($^{79,81}Br$ and ^{127}I) of known velocities. These pulse-heights and, therefore, times-of-flight, were then related to the pulse-heights obtained with a pulser and standard delay cables, giving a relation between time-of-flight and equivalent-delay analogous to the energy vs. pulse-height relations of the previous section. Details of this calibration are given below.

Correction for Velocity Loss in Electron Foil

In order to obtain a zero signal for timing purposes, the iodine and bromine ions had to pass through the thin (≈3μin.) Ni foil described in the previous chapter. An ion of known velocity, v_1, emerging from the analyzer magnet, passes through the Ni foil and loses about 1.5 to 2.0% of its velocity, emerging with velocity, v_2. The time-of-flight of the particle is given by $t_f = \frac{D}{v_2}$. Therefore, in order to know t_f one must determine v_2.

For the energy calibration measurements the Ni foil was left out. The energies measured by the system were the energies that the particles had as they emerged from the analyzer magnet, E_1. Runs also were made under identical conditions with the Ni foil in place. The energies measured in this case are the energies of the particles as they emerge from the Ni foils, E_2. Then, $E_1 - E_2 = \Delta E$, is the energy lost in the

Ni foil by an iodine or bromine ion of given energy. A plot of ΔE vs. E for a typical case is shown in Figure 19. (A dE/dX study of heavy ions in nickel is beyond the scope of this work. However, it might be of interest to note that such a study is in progress at this laboratory (Moak and Brown, 1963).)

For each velocity peak the following calculation was performed: $E_1 = \frac{1}{2} mv_1^2$, $E_2 = \frac{1}{2} mv_2^2$; therefore, $E_1 - E_2 = \Delta E = \frac{1}{2} mv_1^2 - \frac{1}{2} mv_2^2$ and

$$v_2 = \sqrt{v_1^2 - \frac{2E}{m}}.$$

Now there is associated with each velocity peak, located at a specific channel number, a velocity, v_2. This velocity is related to the time-of-flight of the particles through the expression $t_f = \frac{D}{v_2}$. Therefore, we have a relationship between time-of-flight and channel number for a specific run. In order to make the calibration independent of amplifier gains, pulse-height analyzers, etc., a standard, analagous to the pulser in the energy calibration is needed. For this purpose standard delay cables were used.

Delay Cable Standard

In order to obtain reproducible calibration points, equivalent to the pulser points for the energy calibration, delay cables were used. The experimental arrangement is shown in Figure 17. A pulse from a mercury-relay pulser is split at the pulser output. One signal is capacitively coupled to the input of the linear pre-amplifier, as described previously. This signal passes through the coupling transformer of the fast time-pick-off system and produces a start signal for

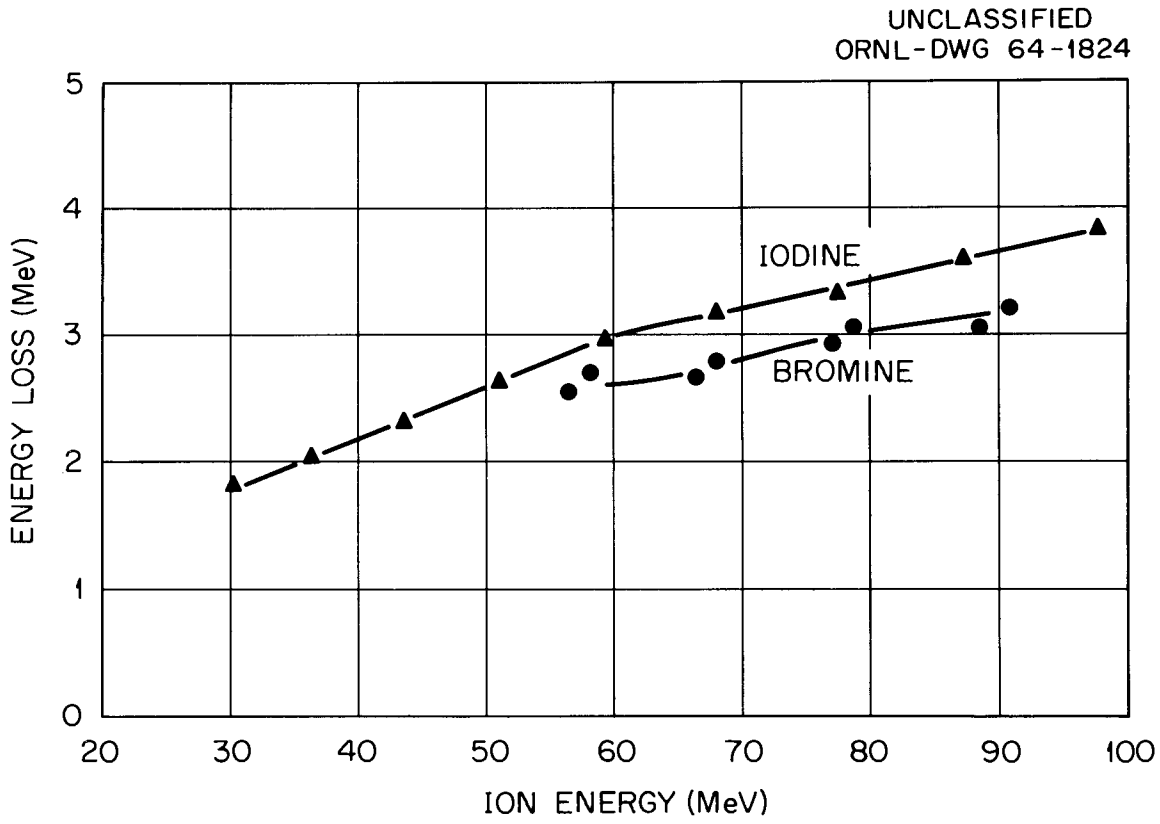

Figure 19. Energy Loss in Nickel Foil vs. Ion Energy.

the TPHC. The other side of the pulser is similarly coupled to a fast amplifier, producing a signal that is passed through calibrated delay cables, and then used as stop signals for the TPHC. It should be emphasized that the known delay cables were in no way part of the absolute calibration of the system, but were merely sources of reproducible time intervals. In this way, relations between time-of-flight and equivalent-delay, analagous to the energy vs. pulse-height relations, were obtained. Figure 20 shows such a curve.

It should be noted that the flight path distance, D, has been calibrated out. The time-of-flight vs. equivalent-delay curve of Figure 20 holds for any flight distance.

Absolute Calibration

For any given run, the absolute time calibration is obtained as follows: under run conditions, equivalent-delay points are put into the pulse-height analyzer. This gives a curve of equivalent-delay vs. channel number. From the time-of-flight vs. equivalent-delay curve, times-of-flight may be associated with specific channels. A least-squares fit is then done to determine the constants in the expression: $t_f = ax_t^2 + bx_t + c$, which is the absolute time calibration for a given run.

III. ABSOLUTE ^{252}Cf VELOCITY SPECTRUM

In order to obtain a universal time-of-flight standard, a time-of-flight measurement was made on the fission fragments from the spontaneous fission of ^{252}Cf.

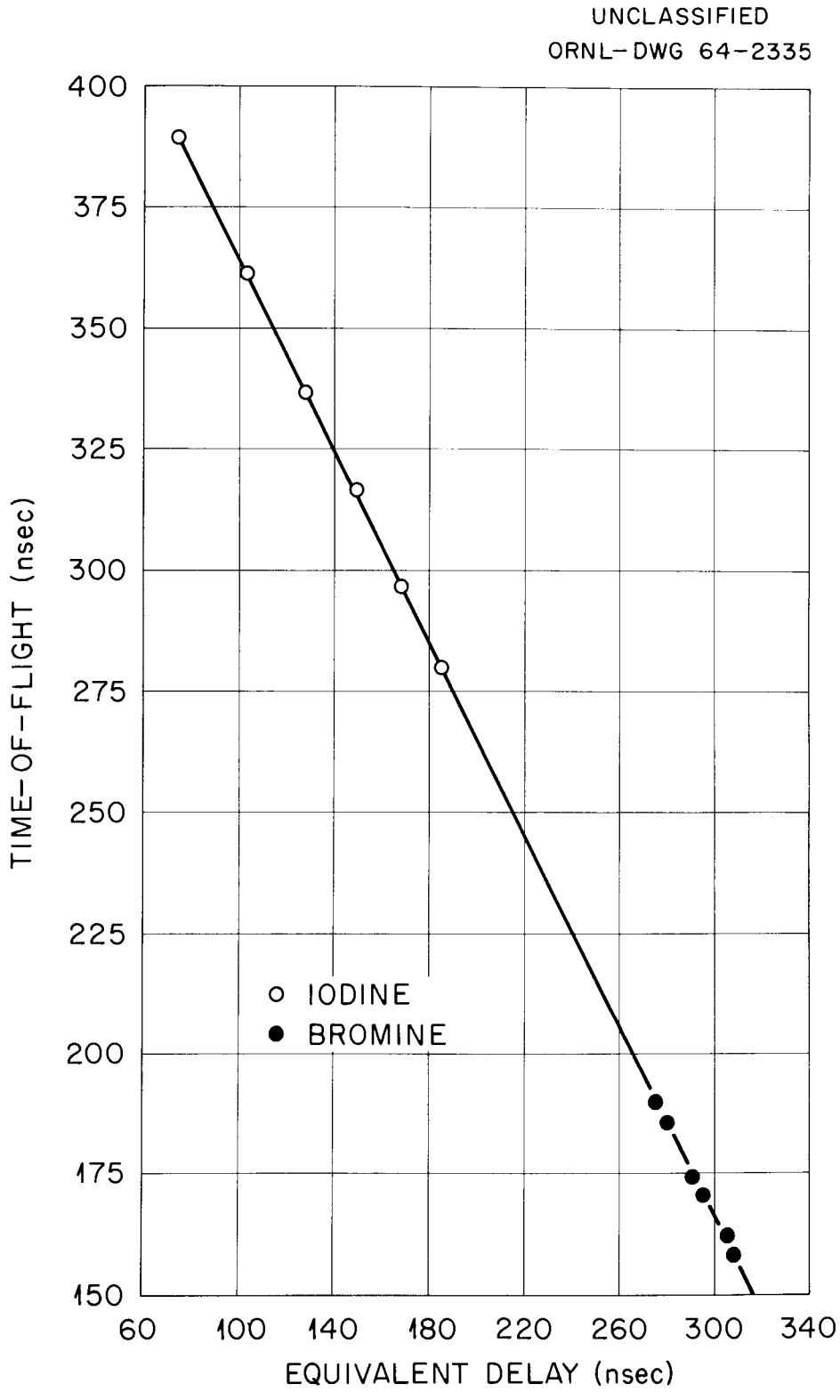

Figure 20. Equivalent-Delay vs. Time-of-Flight for Iodine and Bromine Ions.

Experimental Arrangement

The Cf source was placed in the zero box in the tandem Van de Graaff experiment room immediately after the iodine and bromine runs were completed. The Cf time spectrum was obtained under as nearly the same running conditions as possible as had existed when the iodine and bromine runs were done.

So as not to perturb the velocities of the Cf fission fragments by passing them through the Ni electron foil, the Cf source was mounted directly on the focusing lens plate, replacing the Ni foil (see Figure 2). The Cf source consisted of a platinum foil about 1 inch in diameter and 1 mil thick onto which had been self-deposited about 0.03 μgm of ^{252}Cf. The ^{252}Cf had been deposited onto a spot about 1/4 inches in diameter at the center of the platinum foil. It is probable that the electrons for the zero signal were pulled from the surface of the platinum foil by the very large positive charge of the fission fragment.

All other conditions were as existed during the iodine and bromine runs.

Results

The pulse-height spectrum obtained, including a time scale, is shown in Figure 21. The time scale comes from the expression, $t_f = ax_t^2 + bx_t + c$, where the constants a, b, and c are determined by the calibration methods previously described. Transforming the pulse-height spectrum to velocity, then, one obtains the velocity distribution shown in Figure 22. This transformation is accomplished as follows: the pulse-height spectrum was smoothed by averaging the events in steps of five channels each and drawing the best smooth curve through the

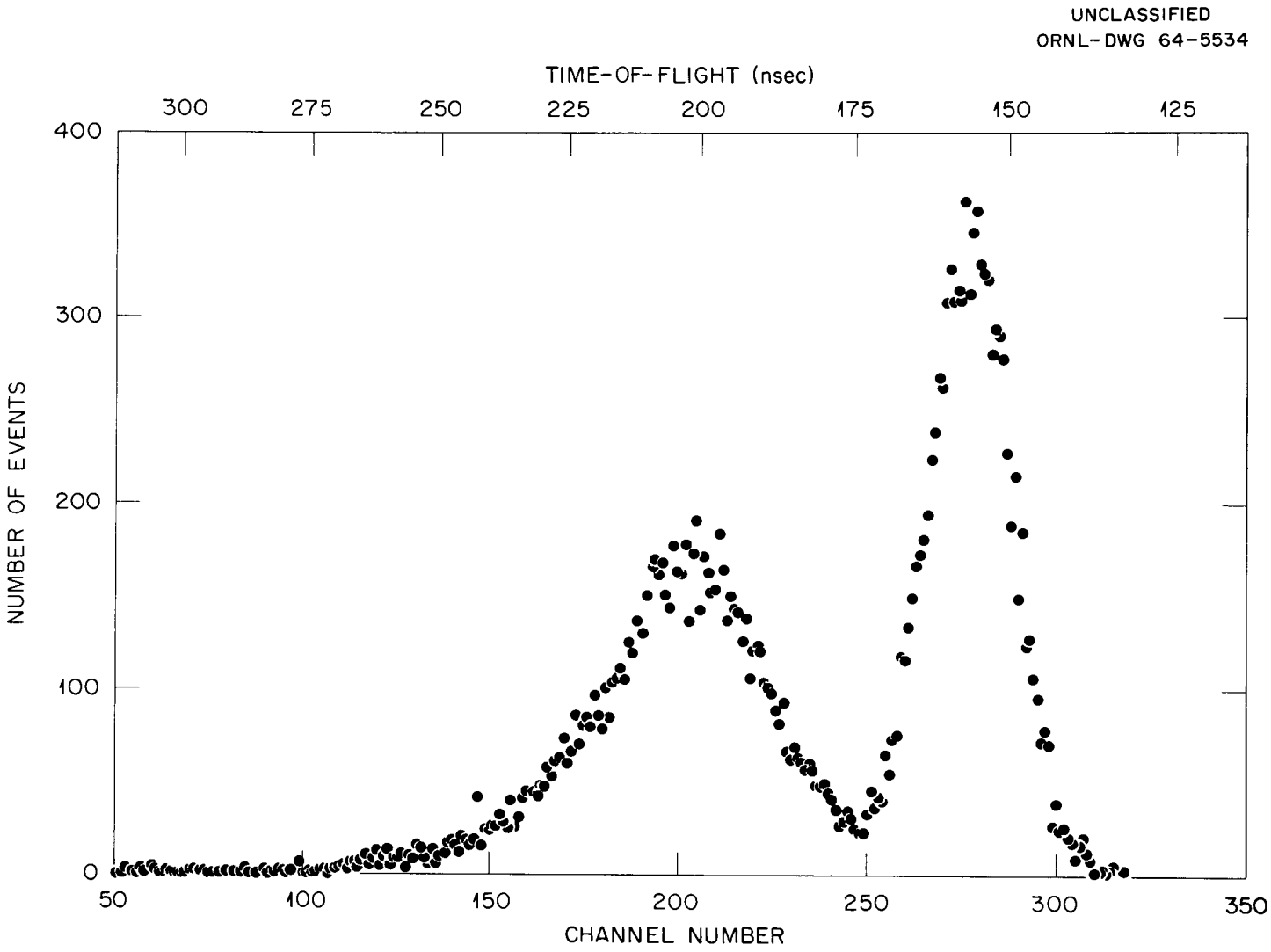

Figure 21. Pulse-Height (Time) Spectrum from ^{252}Cf Absolute Time-of-Flight Experiment.

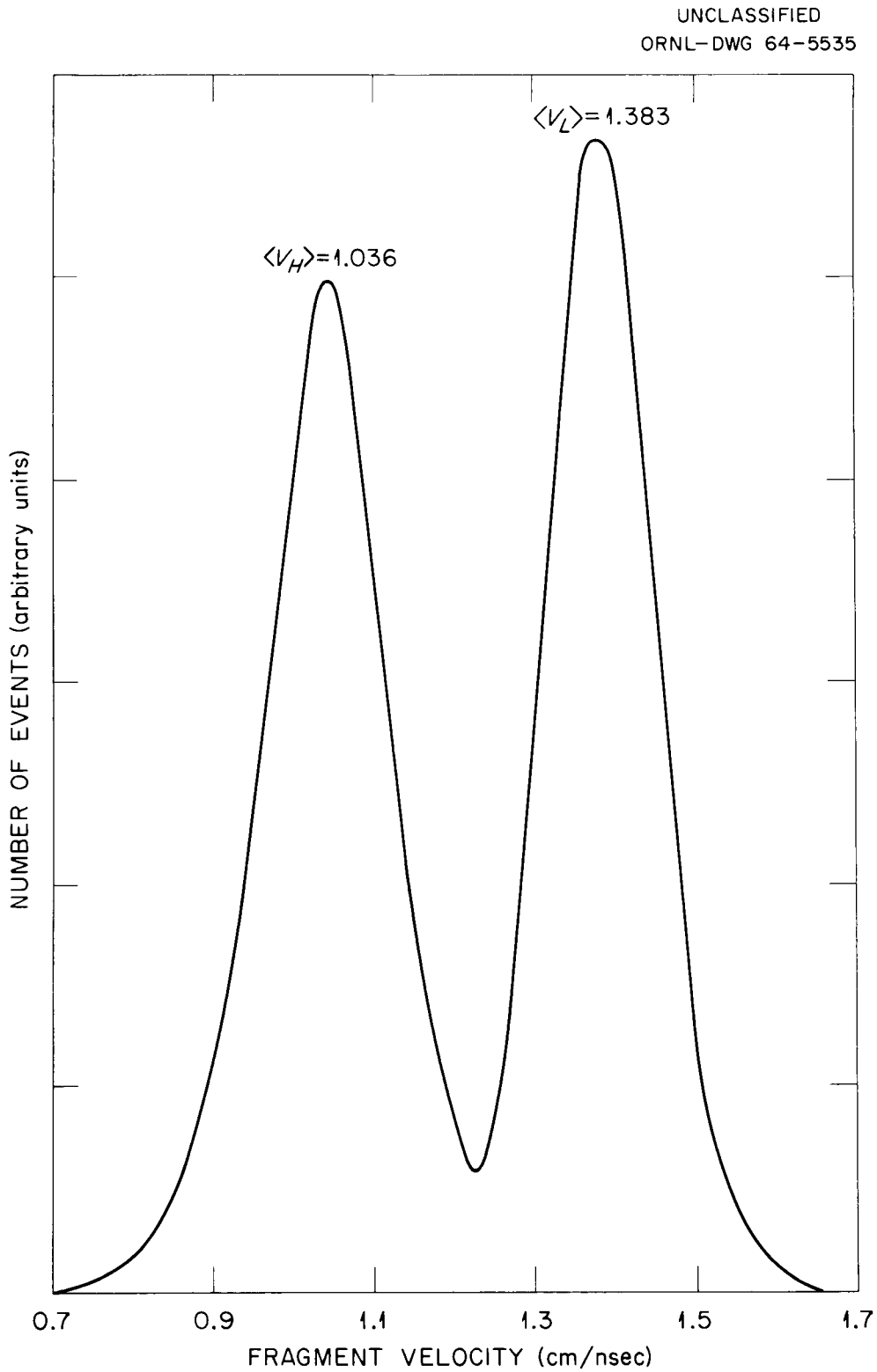

Figure 22. Absolute Velocity Distribution from ^{252}Cf Time-of-Flight Experiment.

resulting points. This smooth function of channel number, F(x), is related to the velocity distribution through the relation, $G(v) = F(x)\frac{dx}{dv}$, where $v = D/t_f$ and $t_f = ax^2 + bx + c$. Carrying out the appropriate differentiation, $\frac{dv}{dx} = t_f^2/D^2(2ax+b)$, and $G(v) = F(x)\ [t_f^2/D^2(2ax+b)]$.

The average light fragment velocity is, $\langle V_l \rangle = 1.383$ cm/nsec; the average heavy fragment velocity, $\langle V_h \rangle = 1.036$ cm/nsec. Averages and standard deviations of several parameters from the present work are tabulated in Table I along with comparable parameters from the double time-of-flight experiments of Whetstone (1963) and Fraser, et al (Fraser, Milton, Bowman, and Thompson, 1963).

For use as an aid in calibrating other time-of-flight apparatus, the values in Table II are given. The peak velocities were determined by locating the velocities that correspond to $G(v) = 0.75\ G(v_p)$. The velocity midway between these two is taken to be the peak velocity.

TABLE I

AVERAGES AND STANDARD DEVIATIONS OF THE VELOCITY, ENERGY AND MASS DISTRIBUTIONS BY DIRECT COMPUTATION AND, IN SOME CASES, GAUSSIAN FITS. ALL QUANTITIES FROM THE PRESENT WORK ARE BY DIRECT COMPUTATION

	This Work	Whetstone		Fraser, et al*	
	Direct Comp.	Direct Comp.	Gaussian Fit	Direct Comp.	Gaussian Fit
E_L(MeV	103.77(105.78)†	105.71	106.16	104.4	105.7
σ_{EL}(MeV)	5.48	5.86	5.66	7.5	5.58
E_H(MeV)	79.37(80.36)†	80.01	80.55	78.3	79.6
σ_{EH}(MeV)	8.23	8.53	8.62	9.5	8.87
V_L(cm/nsec)	1.383	1.375	1.372	1.364	1.370
σ_{VL}(cm/nsec)	0.0693	0.0665	0.063	0.084	0.065
V_H(cm/nsec)	1.036	1.036	1.041	1.023	1.034
σ_{VH}(cm/nsec)	0.0883	0.0795	0.075	0.087	0.077
M_L(amu)	106.00	108.39		107.8	
M_H(amu)	141.94	143.61		144.2	
σ_M(amu)	5.66	5.39		7.27	

†The energy values in parentheses are those from this work corrected for neutron emission by the factors $1 + \bar{\nu}_{L,H}/\overline{M^*}_{L,A}$, where Terrell's (1962) values for $\bar{\nu}$ and $\overline{M^*}$ were used.

*These authors suggest that for comparison w ith other experiments their Gaussian Fit numbers be used.

TABLE II

VALUES OF CF FISSION FRAGMENT VELOCITY AT $\frac{1}{4}$, $\frac{1}{2}$, AND $\frac{3}{4}$ THE MAXIMUM PEAK VALUE

	Heavy Particle Peak Velocity (cm/nsec)	Light Particle Peak Velocity (cm/nsec)
$\frac{1}{4}$ max.	.9045	1.267
$\frac{1}{2}$ max.	.9495	1.298
$\frac{3}{4}$ max.	.9880	1.330
Peak	1.041	1.380
$\frac{3}{4}$ max.	1.089	1.428
$\frac{1}{2}$ max.	1.125	1.459
$\frac{1}{4}$ max.	1.172	1.496

CHAPTER IV

DATA ANALYSIS AND RESULTS

I. DATA ANALYSIS

Acquisition and Initial Handling

As is shown in Figure 4, the data arrive as voltage pulses at a multi-parameter (in this case, two parameter) correlation pulse-height analyzer and are recorded, event by event, on punched paper tape. Later they are transferred to magnetic tape for compilation by a computer. From the event by event correlated data the computer constructs a 256 x 256 matrix, as illustrated by the contour diagram of Figure 23. In this matrix the 256 columns correspond to the 256 channels of a pulse-height distribution recorded on the horizontal axis and the 256 rows to one recorded on the vertical axis. Hence, an event occurring at any of the 256 positions in row ten, for instance, would be recorded as having occurred in Channel 10 of the vertical distribution. The single parameter distributions can be obtained by summing each row or each column. In addition, one may obtain distributions in one of the parameters which occur only at specific values of the other by summing only specific elements in a row or column.

The parameters recorded in this experiment were the pulse-heights proportional to the times-of-flight and energies of fission fragments. As has been pointed out, the energy calibration of the system is mass dependent. To be useful, therefore, the data were transformed from functions of X_e and X_t to functions of M and E.

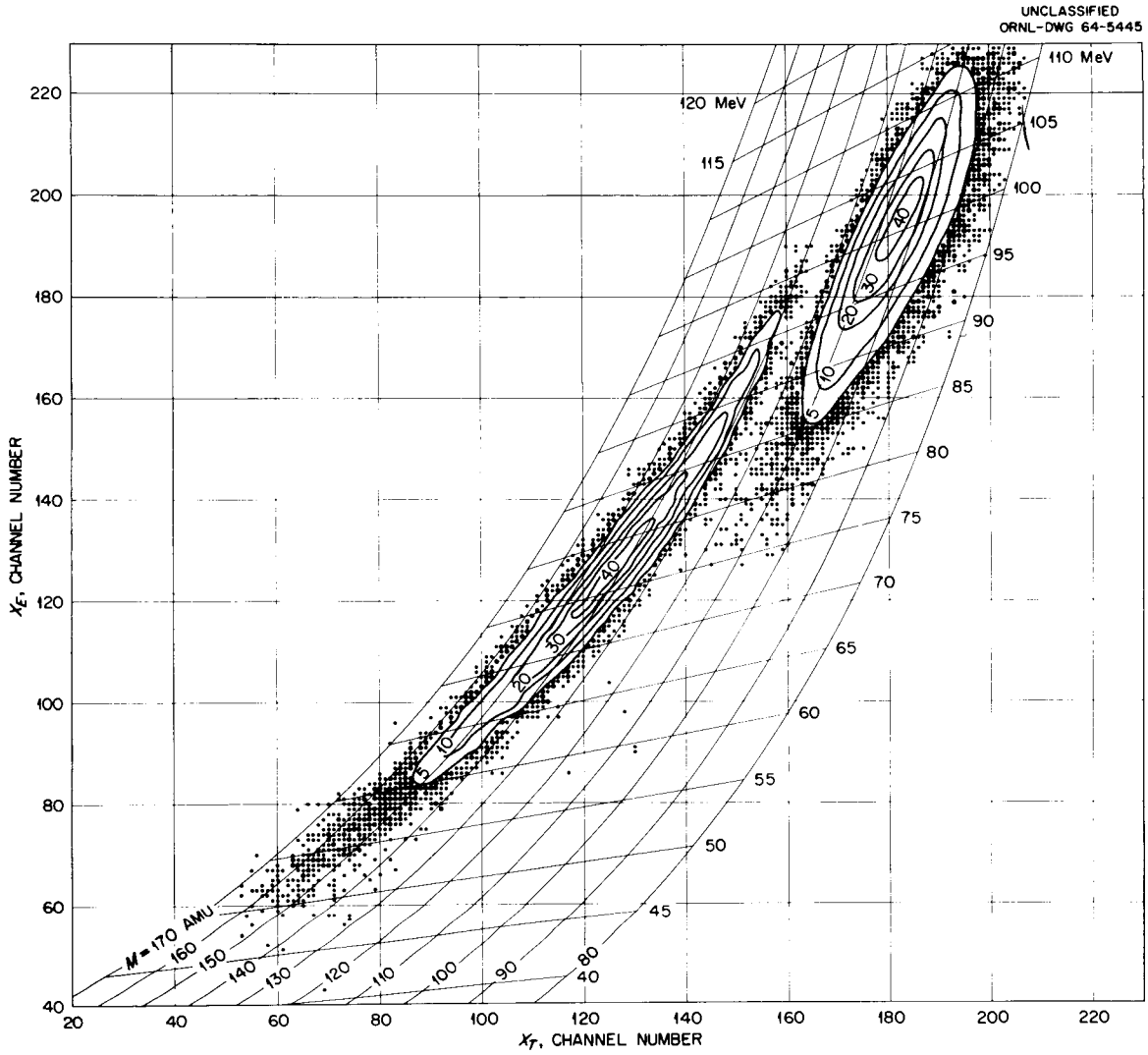

Figure 23. Two Parameter Energy vs. Time-of-Flight Correlation Data for ^{252}Cf Spontaneous Fission Fragments.

Mass, Energy Matrix

By considering the raw data matrix to be a continuous function of X_e and X_t, the Jacobian of the transformation to mass and energy can be calculated analytically. Since a channel represents only about 0.005 of the total width in each dimension, this is a reasonably good assumption. Let $G(X_e,X_t)$ be the distribution function in X_e and X_t and $F(E,M)$ be the distribution function in E and M. Then, $F(E,M)dEdM = G(X_e,X_t)dX_e dX_t$ and $F(E,M) = G(X_e,X_t)J\begin{pmatrix} X_e & X_t \\ E & M \end{pmatrix}$ where the necessary functional relationships are as follows: from the system calibration,

$$E = (a_1 + a_2 M)X_e + b_1 + b_2 M$$

$$t_f = D/v = a_t X_t^2 + b_t X_t + C$$

and the general relation, $E = 1/2\ Mv^2$. The constants in the above equation are, of course, known. These equations may be combined to yield $X_e(E,M)$ and $X_t(E,M)$. Carrying out the appropriate differentiation and algebraic manipulations gives the Jacobian of the transformation. The algebra is cumbersome, though straightforward, and will not be reproduced here. The result is,

$$J\begin{pmatrix} X_e & X_t \\ E & M \end{pmatrix} = \begin{vmatrix} \frac{\partial X_e}{\partial E} & \frac{\partial X_t}{\partial E} \\ \frac{\partial X_e}{\partial M} & \frac{\partial X_t}{\partial M} \end{vmatrix} = \left\{ \frac{MD^2}{\left[8E[b_t^2 - 4a_t(C - \sqrt{\frac{MD^2}{2E}})]\right]} \right\}^{\frac{1}{2}} \left[\frac{(a_1 b_2 - a_2 b_1)M - a_1 E}{EM(a_1 + a_2 M)^2} \right].$$

The numerical transformation is accomplished and the mass, energy matrix constructed as follows. The lowest value of M is selected and paired successively with each possible value of E in steps of 1 MeV.

Then the mass 1 amu higher is chosen and paired with each energy. This procedure is repeated until each mass has been paired with each energy. At each pairing the corresponding values of X_e and X_t are calculated. In general these values of X_e and X_t will not be integral, but will fall between channels, so an interpolation must be done. This interpolation is accomplished by locating the matrix element, $(X_e X_t)$, that corresponds to the nearest integral values of the fractional channel numbers. With this matrix element as the center, the 3 x 3 sub-matrix illustrated below is considered.

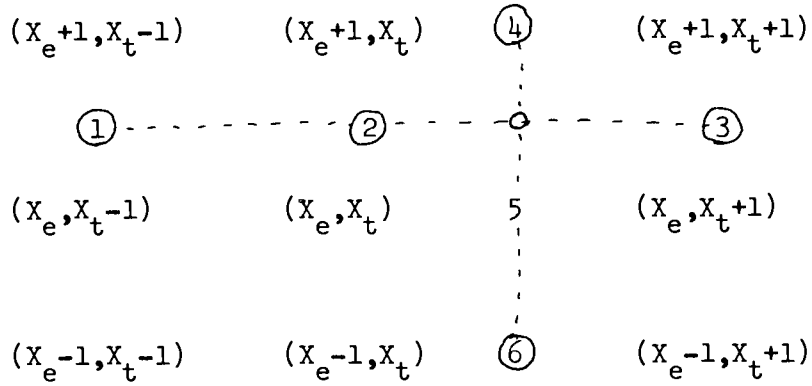

Let the point in the X_e, X_t matrix corresponding to E_i and M_j be designated by O. It is at the point (X_e+f_1, X_t+f_2), where $-\frac{1}{2} \leq f_1 \leq \frac{1}{2}$, and $-\frac{1}{2} \leq f_1 \leq \frac{1}{2}$. The points ①, ②, and ③, then, are at (X_e+f_1, X_t-1), (X_e+f_1, X_t) and (X_e+f_1, X_t+1), respectively. The points ④, ⑤, and ⑥ are at (X_e-1, X_t+f_2), (X_e, X_t+f_2) and (X_e+1, X_t+f_2).

An analytic expression for the function, number of events vs. channel number, is obtained for each column and row of the sub-matrix by fitting a second degree polynomial to the data. This function for column 1, then, allows one to calculate the number of events at point ①; the function for column 2 gives the number of events at point ②,

and so on through points ③, ④, ⑤, and ⑥. Now, second degree polynomials are fitted to the function, number of events at ①, ②, and ③ as a function of X_t, and to the function, number of events at ④, ⑤, and ⑥ as a function of X_e. With each of these expressions the number of events at point *O* is calculated and the average of the two values is taken to be $G(X_e+f_1, X_t+f_2)$. Multiplication by the proper value of the Jacobian, then, gives $F(E_i, M_j)$. The same process is carried out with each E, M pair.

From the mass, energy matrix now, one may obtain the mass and energy distributions, and the average fragment kinetic energy as a function of mass.

II. RESULTS AND DISCUSSION

Unfortunately, there exists no comprehensive theory of fission with which to compare experimental results. However, there are several fission models that have been more or less successful in explaining certain limited aspects of fission. When any of these models seemed to be related to the data presented here, the model was described and the comparison discussed. In the main, however, these data were compared with experimental data obtained by other methods and with pre-neutron experimental data. In particular, fine structure observed in the post-neutron mass distribution from this experiment was compared with the fine structure observed in the pre-neutron mass distribution of Whetstone (1963). These two mass distributions were also used to calculate the average neutron yields as functions of fragment mass; $\bar{\nu}_L(M)$ and $\bar{\nu}_H(M)$, for the light and heavy fragments, respectively.

Fragment Kinetic Energy Distribution

The post-neutron fragment kinetic energy distribution is shown in Figure 24. Also included is the pre-neutron kinetic energy distribution of Whetstone (1963).

The average light and heavy fragment post-neutron kinetic energies from the present work are 103.77 and 79.37 MeV, respectively. These values were corrected for neutron emission by assuming that the only loss in average energy was due to loss in average mass so that each value was corrected by the factor $1 + \bar{\nu}_{L,H}/\bar{M}^*_{L,H}$[†], where $\bar{\nu}$ and $\bar{M}^*$ are the average neutron and fragment masses in amu; both quantities were taken from Terrell (1962). The results are $\langle E_L \rangle_{cor.}$ = 105.78 MeV and $\langle E_H \rangle_{cor.}$ = 80.36 MeV. Whetstone's results are $\langle E_L^* \rangle$ = 105.71 and $\langle E_H^* \rangle$ = 80.01 MeV. It is probably worth noting here that Whetstone's energy distributions are transformations of his time-of-flight data while the energy measurements of this work are completely independent of the time-of-flight measurements. In addition, Whetstone's time-of-flight apparatus was calibrated with known delay cables; the time-of-flight apparatus of this experiment was calibrated with heavy ions of known velocity from the ORNL tandem Van de Graaff accelerator. As was reported in Chapter III, the time-of-flight measurements agree to within about 0.6 per cent. It is felt that the excellent agreement between the average velocities from this work and the average velocities of Whetstone, in light of the widely differing calibration techniques, and the equally excellent agreement between the energy measurements of this work and

---

[†]Throughout this work starred quantities refer to pre-neutron parameters.

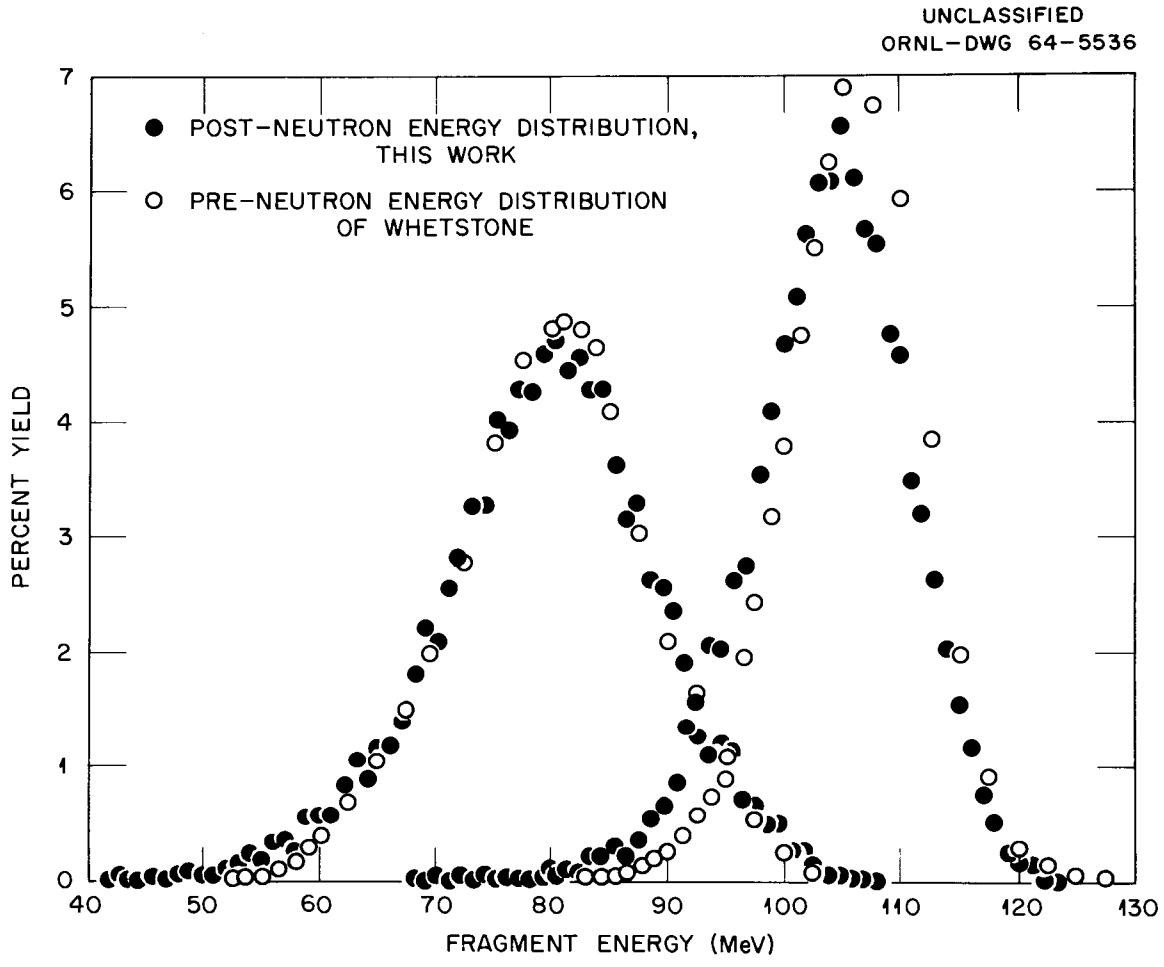

Figure 24. Fission Fragment Kinetic Energy Distributions.

the energies of Whetstone, offer strong evidence for the accuracy of both experiments. For this reason the pre-neutron data of Whetstone was chosen for most of the pre-neutron, post-neutron comparisons, and for the calculation of the average neutron emission per fragment to be discussed in the next section. It should be pointed out here that the pre-neutron parameters of Fraser, et al (Fraser, Milton, Bowman, and Thompson, 1963) calculated by the Gaussian fit method are also in excellent agreement with those from this work and with Whetstone's, as is shown in Table I.

Mass Distribution and Average Neutron Yields

The post-neutron mass distribution, corrected and uncorrected for instrumental resolution is shown in Figures 25 and 26, and tabulated in Table III. The resolution correction was made using the formula,

$$D_{cor.}(M) = D_{meas.}(M) - \frac{\sigma^2(M)}{2} \frac{d^2 D_{meas.}}{dM^2} \qquad (2)$$

which is derived in Appendix C. $D_{meas.}(M)$ is the measured post-neutron mass distribution and $D_{cor.}$ is the distribution after correction. The second derivatives of the measured distribution function were obtained by least squares fitting a second degree polynominal to the distribution at each value of the mass. Each polynominal included five mass points with the mass of interest at the midpoint. The instrumental resolution was measured to be 1.8 and 3.2 amu, FWHM, at masses 80 and 127, respectively. For the purpose of resolution correction, the assumed instrumental resolution was FWHM = 0.025 M. This relation,

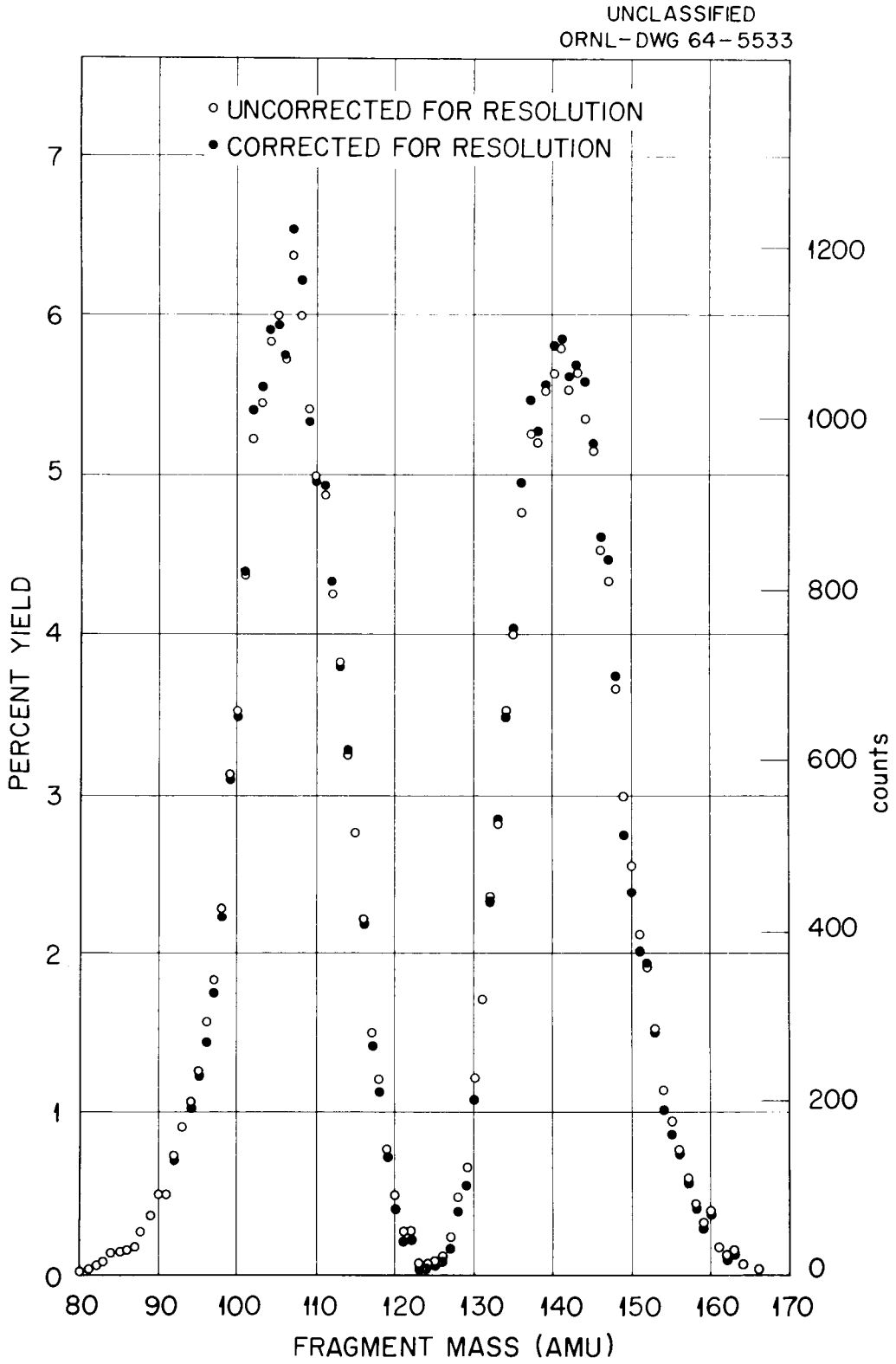

Figure 25. Post-Neutron Mass Distributions, Corrected and Uncorrected for Instrumental Resolution, Linear Plot.

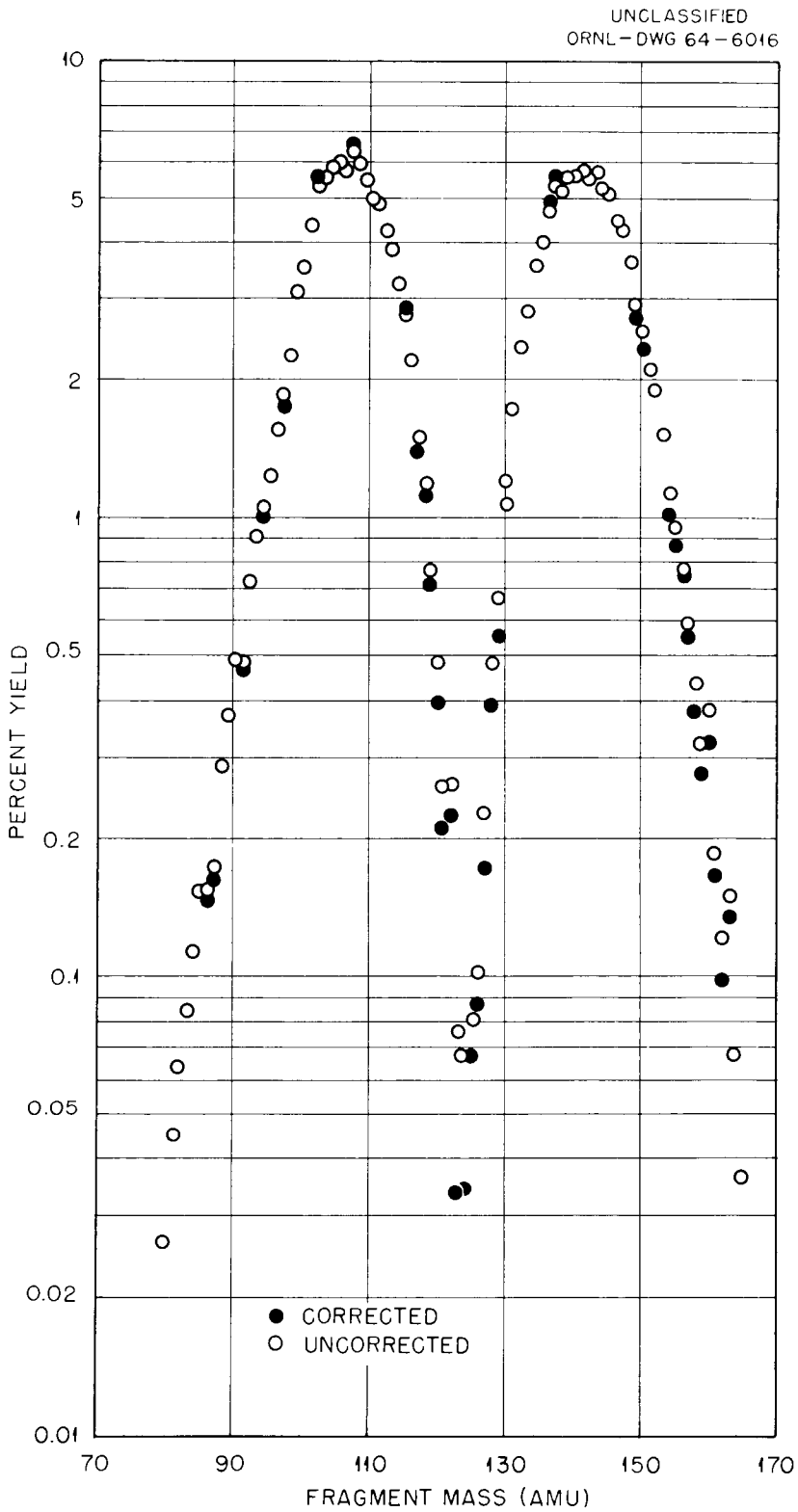

Figure 26. Post-Neutron Mass Distributions, Corrected and Uncorrected for Instrumental Resolution, Logarithmic Plot.

TABLE III

POST-NEUTRON MASS YIELDS, CORRECTED AND UNCORRECTED FOR INSTRUMENTAL RESOLUTION. THE DISTRIBUTION HAS BEEN NORMALIZED TO INTEGRATE TO 200%

Mass	% Yield		Mass	% Yield	
	Corrected	Uncorrected		Corrected	Uncorrected
80		0.026	101	4.394	4.361
81		0.045	102	5.414	5.280
82	0.064	0.065	103	5.556	5.441
83	0.082	0.085	104	5.916	5.828
84	0.115	0.115	105	5.935	5.950
85	0.156	0.156	106	5.742	5.730
86	0.148	0.156	107	6.536	6.377
87	0.163	0.174	108	6.215	5.999
88	0.281	0.289	109	5.348	5.413
89	0.372	0.373	110	4.971	4.993
90	0.487	0.498	111	4.931	4.879
91	0.477	0.492	112	4.327	4.255
92	0.727	0.735	113	3.805	3.821
93	0.911	0.911	114	3.265	3.249
94	1.029	1.052	115	2.810	2.771
95	1.219	1.246	116	2.191	2.214
96	1.535	1.568	117	1.419	1.493
97	1.747	1.836	118	1.123	1.204
98	2.229	2.281	119	0.731	0.772
99	3.098	3.124	120	0.404	0.488
100	3.490	3.535	121	0.216	0.262

TABLE III (continued)

Mass	% Yield		Mass	% Yield	
	Corrected	Uncorrected		Corrected	Uncorrected
122	0.226	0.266	145	5.196	5.155
123	0.035	0.077	146	4.612	4.528
124	0.036	0.069	147	4.471	4.339
125	0.068	0.082	148	3.744	3.673
126	0.088	0.103	149	2.751	2.907
127	0.171	0.230	150	2.384	2.568
128	0.393	0.487	151	2.107	2.128
129	0.557	0.672	152	1.936	1.919
130	1.081	1.203	153	1.510	1.522
131	1.718	1.718	154	1.007	1.130
132	2.329	2.360	155	0.868	0.951
133	2.843	2.282	156	0.758	0.769
134	3.493	3.540	157	0.559	0.592
135	4.031	4.009	158	0.389	0.438
136	4.953	4.760	159	0.283	0.327
137	5.465	5.255	160	0.359	0.381
138	5.266	5.203	161	0.167	0.187
139	5.564	5.533	162	0.100	0.123
140	5.806	5.631	163	0.137	0.152
141	5.859	5.793	164	0.070	0.069
142	5.621	5.536	165		0.037
143	5.685	5.639			
144	5.590	5.359			

along with the assumption that the resolution function is normally distributed about its mean, gives $\sigma(M)$.

Figure 27 is a comparison of the resolution corrected post-neutron mass distribution with the radiochemical mass points of Nervik (1960), Cuninghame (1948), and Glendenin and Steinberg (1955). The general agreement is excellent. The only regions of significant disagreement are in the mass region, 80 to 90 amu and at M = 125, both of which are regions of very low yield. The large bump in the region of mass 80 to 90 amu might be associated with the N = 50 closed shell. The extremely low yield reported by Nervik for mass 125 could be associated with the closed shell Z = 50. More will be said about that presently when neutron emission is discussed.

Figure 28 shows a comparison of the uncorrected post-neutron mass distribution with the pre-neutron mass distribution of Whetstone. The uncorrected distribution is shown because Whetstone's distribution is uncorrected for resolution and it was these distributions that were used to calculate the average neutron emission as a function of mass. This neutron yield curve is also shown in Figure 28, along with the yields calculated by Terrell (1962) and obtained experimentally by Whetstone (1959) and by Bowman, et al (Bowman, Milton, Thompson and Swiatecki, 1963).

The average neutron yield as a function of fragment mass was calculated by the method of cumulative yields, as described by Terrell (1962) and illustrated by Figure 29.

As Whetstone points out, there are four significant departures from a smooth curve on the steep sides of his pre-neutron mass distribution. These occur for the mass pairs 123-129, 118-134, 112-140 and

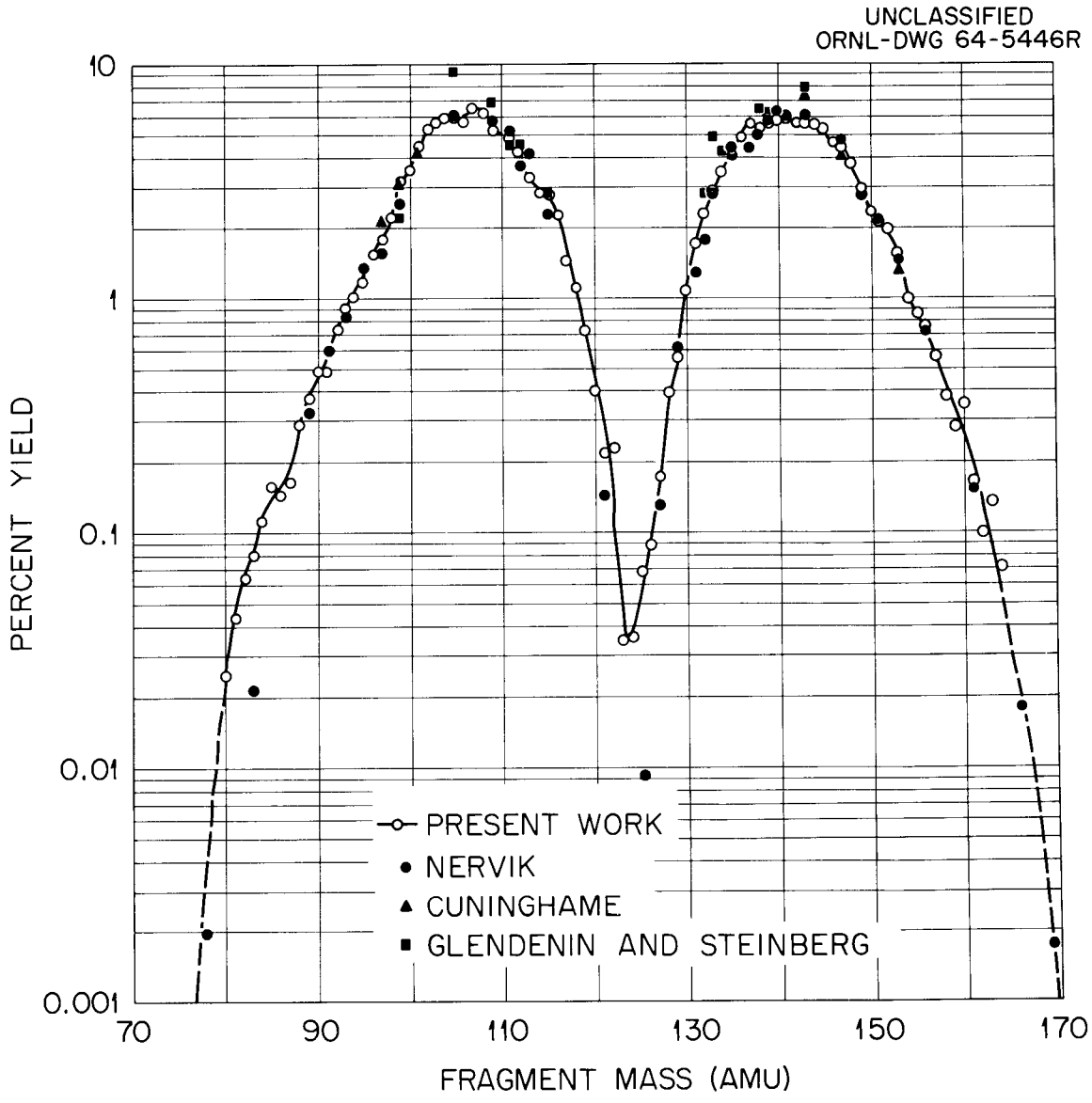

Figure 27. Post-Neutron Mass Distribution Compared with Radiochemical Results.

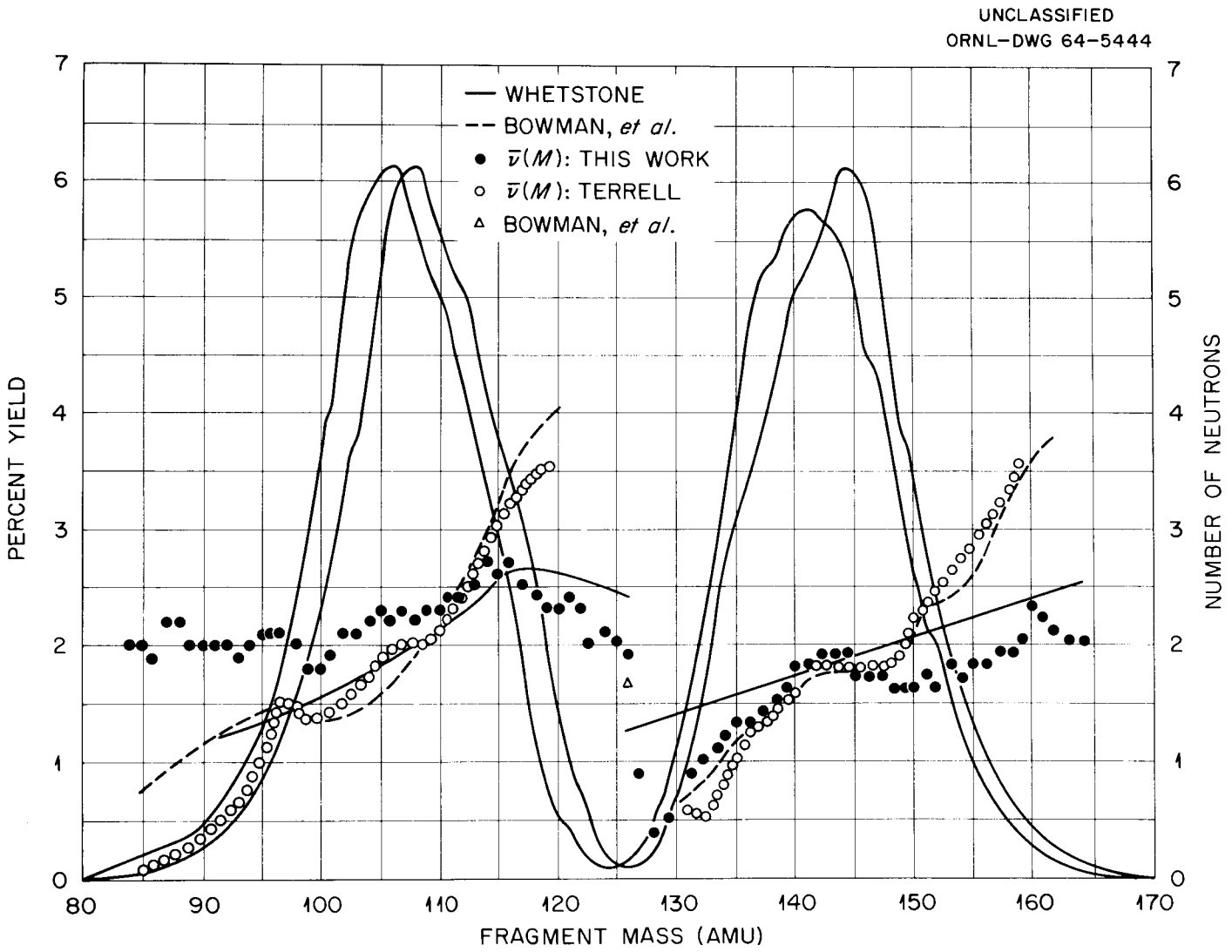

Figure 28. Average Neutron Yield Shown with Pre- and Post-Neutron Mass Distributions.

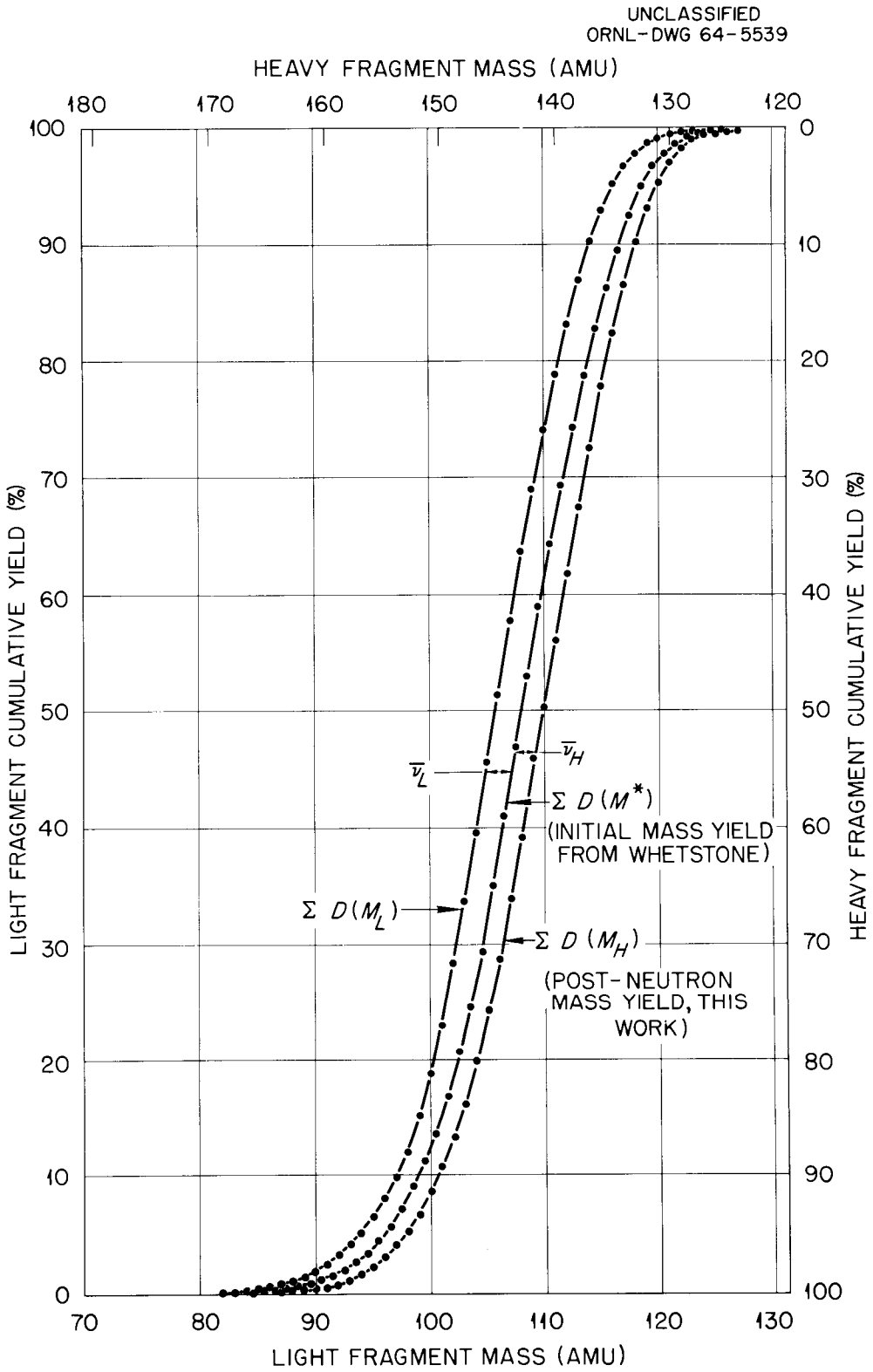

Figure 29. Illustration of the Method of Cumulative Yields for Calculating $\bar{\nu}(M)$ from Mass Distributions.

103-149. The initial, or pre-neutron, mass yield curve must, of course, be symmetric about mass 126. It is rather remarkable that each of these departures is reproduced at the appropriate place in the post-neutron mass distribution with the exception of the one that should occur near mass 133 and this is in a region where the neutron yield increases rather sharply, probably because of the N = 82 closed shell near M = 134. In fact, the light fragment peaks are strikingly similar in shape and this is reflected in the somewhat flat distribution obtained for the neutron yield from the light fragments.

It has been suggested that the fine structure observed in the mass distributions from the low energy fission of heavy nuclei might be due to closed shell effects (see for instance Milton and Fraser, 1958). However, Faissner and Wildermuth (1964) have suggested that the entire mass distribution might be due to closed shell effects. Their cluster model of fission predicts that the fission barrier is lower for a nucleus with unbroken clusters of magic numbers (Z = 50, N = 50, 82) of nucleons. The number of excess nucleons is assumed not to affect the fission probability so that the predicted mass distribution for a fissioning nucleus with $N \geq 132$ is a region of allowed light fragments and a region of allowed heavy fragments. Each mass within a region is equally probable. The lower limit of the heavy fragment region is at $M_H^* = 132$ ($Z_H^* = 50$, $N_H^* = 82$), and, since $M_H^* + M_L^* = A$, where A is the mass number of the fissioning nucleus, the upper limit of the light fragment region is at $M_L^* = A - 132$. The lower limit of the light fragment region, and, therefore, the upper limit of the heavy fragment region,

is determined by a combination of the magic $N_L^* = 50$ and a Z_L^* that depends on the proton to neutron ratio of the original nucleus. For $N < 132$ in the initial nucleus symmetric fission is predicted, in qualitative agreement with experiment.

The fine structure in the mass distributions appears to be associated with the formation of the energetically favored even-even nuclei. The relation between fine structure in fragment kinetic energy distributions and even-even mass surfaces has been discussed in some detail (Milton and Fraser, 1962; Fraser, Milton, Bowman and Thompson, 1963; Thomas and Vandenbosch, 1964). Figure 30 is a plot of the available energy in the spontaneous fission of ^{252}Cf as a function of the even primary fragment masses, for given even Z; from the table of Milton (1962). Also shown is the pre-neutron mass distribution of Whetstone. The pre-neutron mass distribution and available-energy curves are, of course, symmetric about $M^* = 126$. The correlation between the energetically favored masses and the fine structure in the mass distribution is rather striking. It seems quite likely that the fine structure in the pre-neutron mass distribution is due in large part to the formation of energetically favored even-even nuclei and that the fine structure in the post-neutron mass distribution is due to the fine structure in the pre-neutron distribution.

The average neutron yield is in good general agreement with the other yields shown in Figure 28. The only regions of appreciable disagreement are again in the regions of very low mass yield where the uncertainties are large. Terrell's neutron yield curve was obtained by fitting a curve to the radiochemical points and doing a cumulative

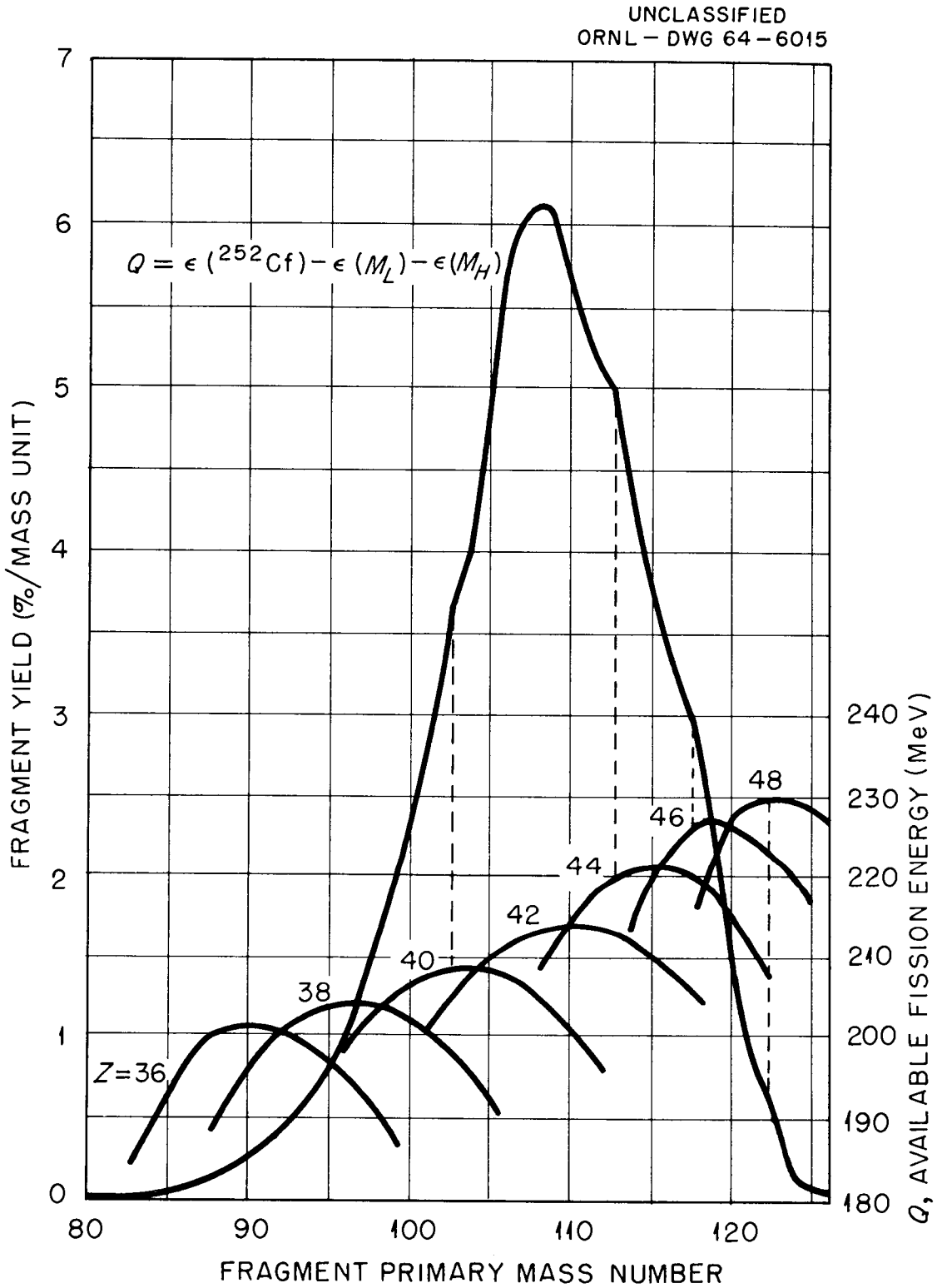

Figure 30. Comparison of Structure in Pre-Neutron Mass Distribution with Available-Energy Curves for Even-Even Fragments.

yield calculation. It is quite possible therefore, that the disagreement between Terrell's curve and the one from this work in the mass region 80 to 90 amu could be due to the disagreement between the radiochemical mass distribution and the one from this work in that region. The measured neutron yields lie about midway between the calculated ones.

Whetstone's neutron yield distribution shows a sharp discontinuity at symmetric fission, M* = 126. This is in qualitative agreement with the extremely low yield obtained by Nervik (1960) for mass 125 (0.0093 per cent) and the much larger yield at mass 127 (0.13 per cent). He is able to explain this discontinuity as well as the asymmetric mass yields with his so-called "neck theory" of fission (Whetstone, 1959). This model envisions two large masses connected by a long thin neck as illustrated by Figure 31. The masses will, in general, be unequal so that if it is assumed that rupture at the center of the neck is most probable, this will give the observed asymmetric mass distribution. In addition, rupture at the center of the neck gives to each fragment about half of the deformation energy of the neck so that the fragments should emit about equal numbers of neutrons at the most probable mass split, again in good agreement with observation. For near symmetric fission the rupture occurs very near the larger mass, which gives virtually all of the deformation energy to the smaller mass and implies that far more of the prompt neutrons would be emitted by the light particle, which, of course, would explain a discontinuity in neutron yield near symmetry. However, the results of this work and the measurements of Bowman, et al (Bowman, Milton, Thompson, and Swiatecki, 1963) indicate that no such discontinuity exists. Also, this work does not reproduce the very low

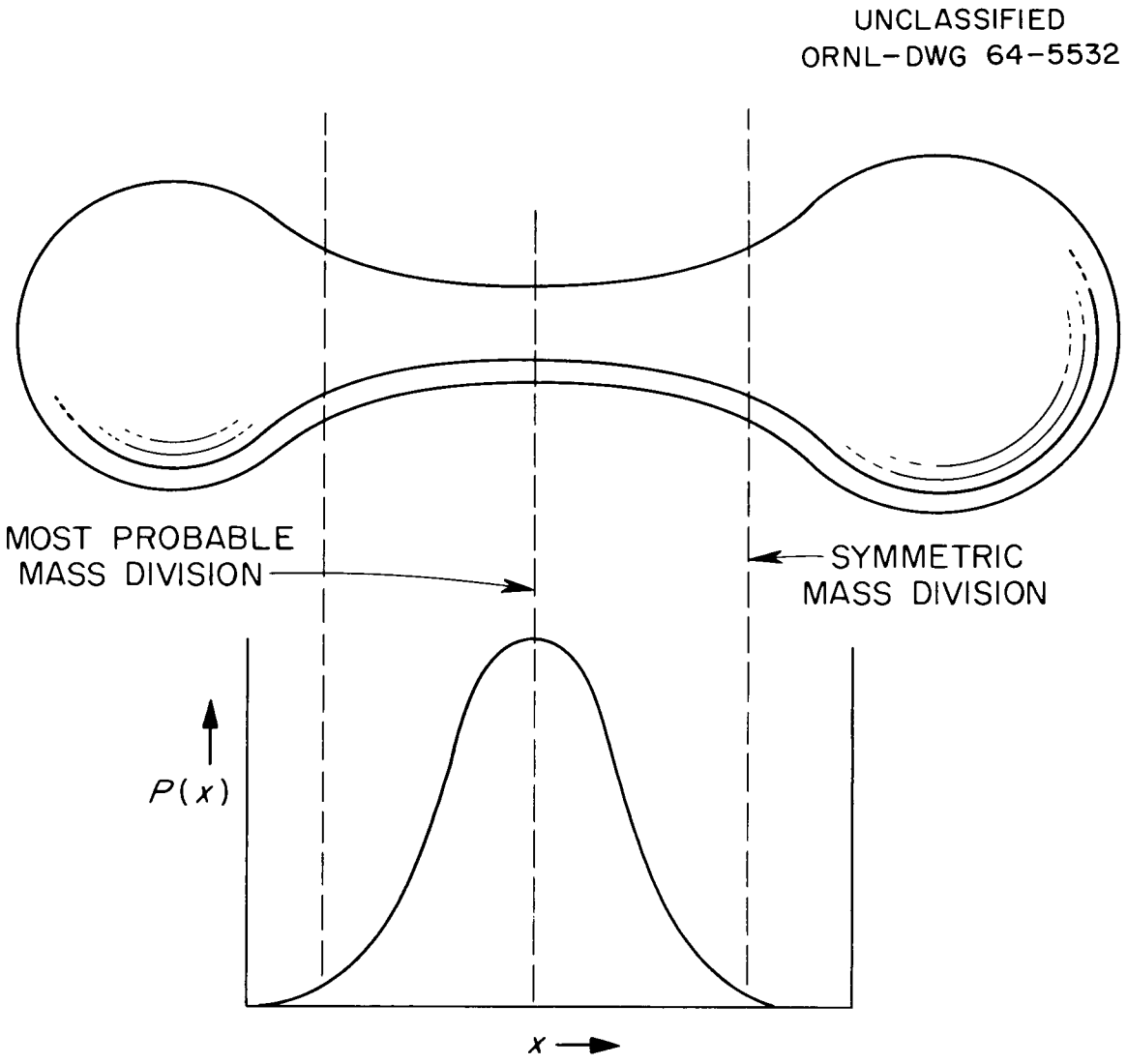

Figure 31. Illustration of Whetstone's Neck Theory.

yield at mass 125. Of course, instrumental resolution can greatly fill in a deep narrow valley and the resolution correction used was an approximation. The resolution correction was checked for the mass points 120-130, however, by using the corrected mass distribution to determine the second derivatives and applying the correction again. These new corrections were insignificantly different from the original corrections. It, thus, appears that if the neck theory is to survive some new features must be incorporated into it. As Whetstone points out, one such feature might be the assumption that a small fraction of the fissions occur as a separate fission mode in which symmetric fission is dominant. Experimental tests for this assumption will be discussed in the next chapter.

Average Fragment Kinetic Energy as a Function of Fragment Mass

Figure 32 shows the average fragment kinetic energy for each fragment mass. The pre-neutron data of Whetstone (1963) are also shown.

Probably the most important feature of this curve from the present experiment is the confirmation of the rather dramatic decrease in fragment kinetic energy near symmetric fission, M = 126. This sharp decrease suggests the existence of a separate fission mode in which the mass split is predominantly symmetric and the fragment kinetic energy unusually low, and appears to be in disagreement with a statement by Vandenbosch (1963) in his discussion of a similar kinetic energy decrease at symmetry in the thermal neutron fission of ^{233}U, ^{235}U, and ^{239}Pu. Coulomb excitation studies indicate (Stelson and McGowan, 1958) that nuclei in the mass range 112-120 are abnormally soft toward deformation. Vandenbosch points out that the symmetry masses of ^{234}U,

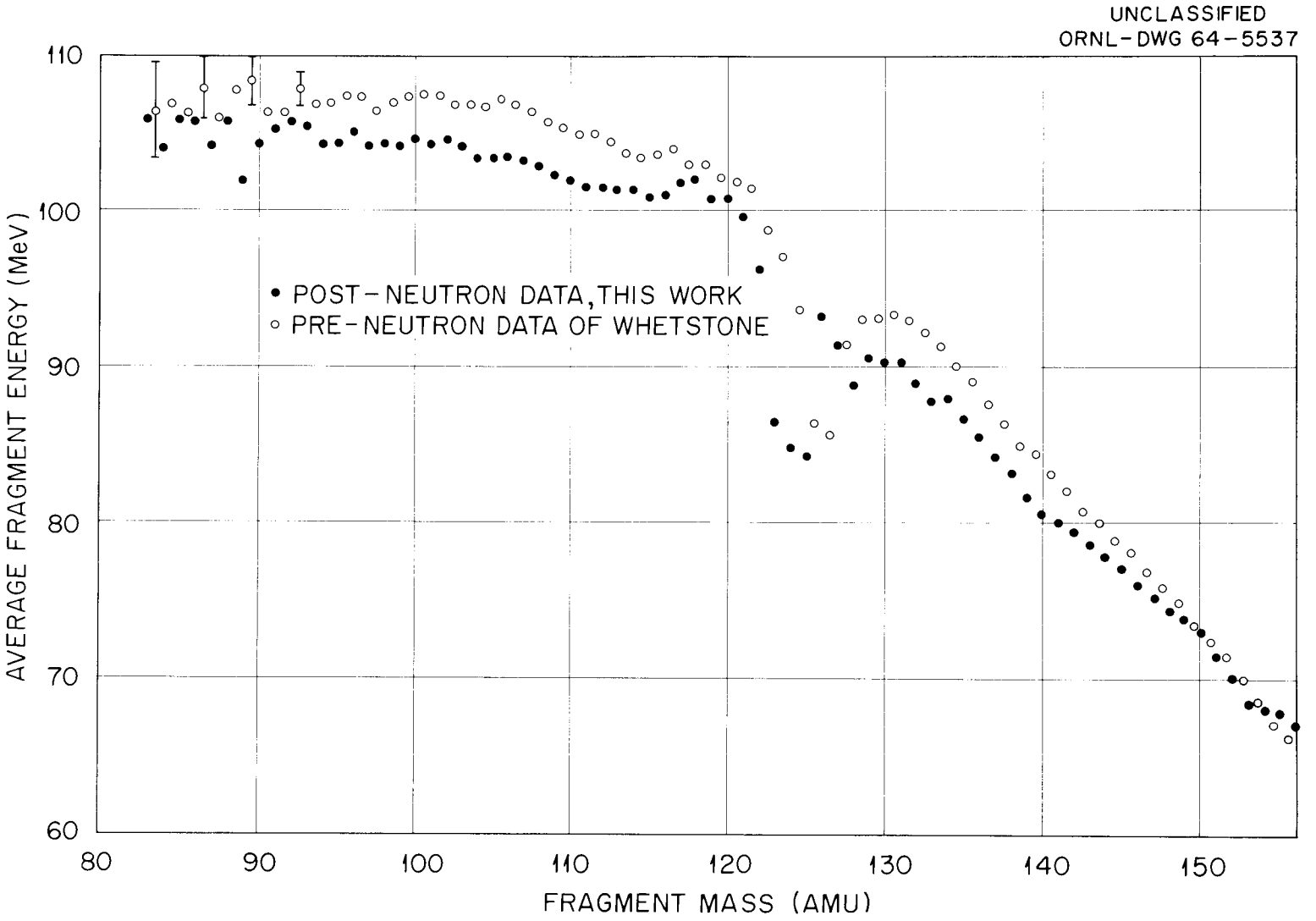

Figure 32. Average Fragment Kinetic Energy as a Function of Fragment Mass.

^{236}U, and ^{240}Pu are in this region of softness and suggests, as a working model, that just at the instant of scission the fission fragments be thought of as tangent spheroids. Then, if it is assumed, as is usually the case, that the kinetic energy of the fragments is just the Coulomb potential energy at the instant of scission, having both fragments deformed produces less kinetic energy than does the situation in which one or both of the fragments are more nearly spherical. In light of this softness toward deformation in the mass range 112-120 amu, Vandenbosch suggests that the observed decrease in kinetic energy near symmetry in the fission of ^{234}U, ^{236}U, and ^{240}U has nothing to do with symmetric fission but is caused by the accidental occurrence of the symmetric masses in this region of unusual softness. Quantitative calculations were made with this model by assuming tangent spheroids with major and minor axes A_1, A_2 and B_1, B_2. The potential energy of the system was minimized with respect to A_1/B_1 and A_2/B_2 simultaneously for each mass ratio. The calculations show no decrease in kinetic energy near symmetry for ^{252}Cf. However, it is doubtful that the model is good enough to distinguish sharply between fragments of mass 120 and those of mass 126 and it is felt that the quantitative disagreement does not detract appreciably from his qualitative arguments. Unfortunately this still leaves the question of the existence of a separate fission mode at symmetry quite up in the air. Much more data are needed on the fission of nuclei of mass around 200 amu, both because the symmetric fragments would be far removed from the region of high deformability and because many nuclei in this region are preferentially symmetric fissioners.

A rather striking feature of the data in Figure 32 is the more or less constant value of the average kinetic energy of the light fragment in both the pre-neutron and post-neutron data. It should be noted that somewhat flat curves for both the pre- and post-neutron average kinetic energies, displaced from each other by a more or less constant amount, is quite consistent with the rather flat curve obtained for the average number of neutrons emitted as a function of the light fragment mass.

The overlapping of the curves in the region about mass 150 probably means that Whetstone's mass resolution is better there than our measured resolution of about 0.025 M = 3.75 amu, and that our average energies in this region are too large because of resolution spreading in the mass distribution. If this is the case, then our average neutron emission, which was calculated using the uncorrected mass distributions, is probably too small in this region and our curve should probably be in better agreement with the other values than is shown in Figure 28.

CHAPTER V

CONCLUSIONS

Probably the most important contributions of this experiment to the field of fission physics are the post-neutron kinetic parameters discussed in detail in the previous chapter. However, a contribution of almost equal importance must be the development of the experimental techniques and methods of analysis for the simultaneous measurement of energies and times-of-flight.

Of particular importance is the energy calibration of the solid-state detectors. The good agreement between this work and other experiments is strong evidence that the indicated linear mass dependence of the energy vs. pulse-height relation is valid over the range of fission fragment masses. This, along with the techniques for taking both a linear (energy) and fast time signal from the same solid-state detector, provides the experimentalist with a powerful tool for the study of fission fragment kinetics. It will now be possible to obtain both pre-neutron and post-neutron data simultaneously.

The most obvious extension of this work would be the replacement of the remote detectors in existing time-of-flight apparatus with semiconductor detectors and beginning systematic double time-of-flight, energy correlation measurements on the available neutron fissioning nuclei. Practically all existing double time-of-flight apparatus for studying nuclear fission are more or less permanently installed at various nuclear reactors.

In addition to data on neutron induced fission, much more experimental data are needed on charge particle fission, especially of nuclei in the mass region around 200 amu. In this region fission is predominantly symmetric and the symmetry mass is fairly far removed from the 112-120 amu region of extreme softness toward deformation. Also, liquid drop calculations have been reasonably successful in predicting some of the features of fission in this mass region (Burnett, 1963; Cohen and Swiatecki, 1962a and 1962b; Nix, 1963).

It is suggested that for a long and systematic study of charged particle fission where it would be desirable to measure both pre- and post-neutron parameters, a valuable experimental tool would be a three parameter system in which an energy correlation is done along with one time-of-flight measurement. It has been shown that double time-of-flight measurements are fundamentally more sound than energy correlations for obtaining pre-neutron data (Bowman, Wegner and Whetstone, 1964). However, the necessarily long flight paths of double time-of-flight apparatus along with the perturbing effects of neutron emission (Lide, 1962) require large count rates at the source, or very long periods of data taking. Also, double time-of-flight apparatus is bulkier and more cumbersome to handle than is energy correlation apparatus. It would be rather inconvenient to set up and take down regularly, which would probably be the case if a long systematic study of charged particle fission were undertaken.

On the other hand, it has been shown that timing with two solid-state detectors permits an absolute time resolution of about 0.5 nsec (Williams, Kiker and Schmitt, 1964). This means that a flight path of

75 to 100 centimeters would be adequate. Then a piece of apparatus only slightly more complicated than a well collimated, 1 meter long by 5 centimeter diameter aluminum pipe would constitute the entire mechanical part of the experiment. One end of the pipe would contain a thin source of fissile material and a semiconductor detector from which would be taken a linear signal and zero time signal. The remote fragment detector would be at the other end of the pipe and would give a linear signal and "stop" time signal. The system would be small and could be set up and taken down easily and quickly as time would become available on the large charged particle accelerators. Then a long and systematic study of charged particle fission, measuring both pre- and post-neutron parameters would be quite feasible.

REFERENCES

Bowman, H. R., Wegner, H. E., and Whetstone, S. L., Jr., 1964, "A Comparison of Fission Fragment Measurements Made with Double-Energy and Double Velocity Techniques" (to be published).

Bowman, H. R., Milton, J. C. D., Thompson, S. G., and Swiatecki, W. J., 1963, Phys. Rev. 129, 2133.

Brunton, D. C., and Hanna, G. C., 1950, Can. J. Res. A28, 190.

Brunton, D. C., and Thompson, W. B., 1950, Can. J. Res. A28, 498.

Burnett, D. S., 1963, Kinetic Energy and Mass Distributions for Nuclear Fission at Moderate Energy, (PhD Thesis), University of California, UCRL-11006.

Cohen, S., and Swiatecki, W. J., 1962a, Ann. Phys. 19, 67.

____, 1962b, The Deformation Energy of A Charged Drop: Part V: Results of Electronic Computer Studies, UCRL-10450.

Cuninghame, J. G., 1948, J. Inorg. and Nuclear Chem. 6, 181.

Faissner, H., and Wildermuth, K., 1964, Cluster Model of Nuclear Fission: I. Asymmetric Mass Distributions (submitted for publication in Nuclear Physics).

Fraser, J. S., Milton, J. C. D., Bowman, H. R., and Thompson, S. G., 1963, Can. J. Phys. 41, 2080.

Frisch, O. R., 1939, Nature 143, 276.

Glendenin, L. E., and Steinberg, E. P., 1955, J. Inorg. and Nuclear Chem. 1, 45.

Glendenin, L. E., Steinberg, E. P., Inghram, M. G., and Hess, D. C., 1951, Phys. Rev. 84, 860.

Hahn, O., and Strassman, F., 1939a, Naturwiss 27, 11.

____, 1939b, Naturwiss 27, 89.

Henderson, M. C., 1940, Phys. Rev. 58, 774.

Jentschke, W., and Prankl, F., 1939, Naturwiss 27, 134.

Joliot, F., 1939, Comp. rend. 208, 341, 647.

Knipp, J. K., and Ling, R. C., 1951, Phys. Rev. 82, 30.

Leachman, R. B., 1952, Phys. Rev. 87, 444.

Leachman, R. B., and Schmitt, H. W., 1954, Phys. Rev. 96, 1366.

Leachman, R. B., and Shafer, W. D., 1955, J. Can. Phys. 33, 357.

Lide, R. W., 1962, The Effect of Prompt Neutrons on the Distribution of Time-of-Flight of Fission Fragments, ORNL-3338.

Meitner, L., and Frisch, O. R., 1939, Nature 143, 239, 471.

Milton, J. C. D., 1962, Fission Energy Tables and an Application to Nuclear Charge Division, UCRL-9883 Rev.

Milton, J. C. D., and Fraser, J. S., 1958, Phys. Rev. 111, 877.

____, 1962, Can. J. Phys. 40, 1626.

Moak, C. D., and Brown, M. D., 1963, Phys. Rev. Letters 11, 284.

Moak, C. D., Neiler, J. H., Schmitt, H. W., Walter, F. J., and Wells, G. F., 1963, Rev. Sci. Instr. 34, 853.

Mruk, W. F., 1963, The Principles and Measurement of Fission Fragment Times-of-Flight, (Ph.D. Thesis), University of Tennessee.

Nervik, W. E., 1960, The Spontaneous Fission Yields of ^{252}Cf, UCRL-5584.

Nix, J. R., 1963, Estimates of Fission-Fragment Kinetic-Energy Distributions on the Basis of the Liquid Drop Model, UCRL-10695.

Schmitt, H. W., and Leachman, R. B., 1956, Phys. Rev. 102, 183.

Schmitt, H. W., Neiler, J. H., Walter, F. J., and Chetham-Strode, A., 1962, Phys. Rev. Letters 9, 427.

Schmitt, H. W., Neiler, J. H., Walter, F. J., Gibson, W. M., and Thomas, T. D., 1964, (to be published).

Schmitt, H. W., Walter, F. J., Neiler, J. H., Moak, C. D., Gibson, W. M., and Thomas, T. D., 1963, Response of Silicon Solid-State Detectors to Heavy Ions and Fission Fragments, in Physics Division Annual Report, ORNL-3425.

Stein, W. E., and Whetstone, S. L., Jr., 1958, Phys. Rev. 110, 476.

Stelson, P. H., and McGowan, F. K., 1958, Phys. Rev. 110, 489.

Terrell, J., 1962, Phys. Rev. 127, 880.

Thode, H. G., 1960, Advances in Inorganic Chemistry and Radiochemistry, edited by H. J. Emeleus and A. G. Sharpe, Academic Press, Inc. New York.

Thode, H. G., and Graham, R. L., 1947, Can. J. Res. A25, 1.

Thomas, T. D. and Vandenbosch, R., 1964, Phys. Rev. 133, B976.

Vandenbosch, R., 1963, Nuclear Physics 46, 129.

Walter, F. J., Schmitt, H. W., and Neiler, J. H., 1964, Phys. Rev. 133, B1500.

Whetstone, S. L., Jr., 1959, Phys. Rev. 114, 581.

____, 1963, Phys. Rev. 131, 1232.

Williams, C. W., and Biggerstaff, J. A., 1964, Nuclr. Instr. Methods 25, 370.

Williams, C. W., and Neiler, J. H., 1962, IRE Trans. on Nuclr. Sci. NS-9.

Williams, C. W., Kiker, W. E., and Schmitt, H. W., Correlated Energy and Time-of-Flight Measurements of Fission Fragments with Semiconductor Detectors: System Design and Performance, (to be published in Rev. Sci. Instr.).

APPENDIX A

PRODUCTION AND MAGNETIC ANALYSIS OF HEAVY IONS

Much of the following discussion was taken from Moak, Neiler, Schmitt, Walter, and Wells (1963).

Ion Production

Negative ions are introduced into the first stage of the tandem Van de Graaff accelerator in the usual manner and accelerated to energies of several MeV (Figure 3). They then pass through the gas-filled stripper-canal and emerge as quadruply--or quintuply--charged positive ions. These are accelerated in the second stage of the tandem in which there is a small quantity of gas. As the particles accelerate, encounters with gas atoms remove more electrons; and the particles, being more highly charged, accelerate more rapidly. This greater acceleration increases the probability of the removal of more electrons, thus causing an even greater acceleration. This compounding leads to positive ions of charge up to about +20 and energies up to 120 MeV. Since the charge-changing is random, the energy spectrum of the emerging ions is continuous, ranging from about 30 MeV to 120 MeV.

Magnetic Analysis

The following discussion will be in terms of selecting groups of ions of given energies. Obviously, for ions of constant mass, one also selects groups of ions of given velocities.

The ions emerging from the second stage of the tandem Van de Graaff accelerator are passed through a 90° bending magnet. A charged

particle of mass, M; energy, E; and charge, q; passing through a magnetic field of strength, H; follows a curved path with radius of curvature, ρ; and must satisfy the equation, $ME/q^2 = H^2\rho^2$. Or, this may be written, $ME/q^2 = k\nu^2$, where k is a constant that depends only on the properties of the magnet and ν is the frequency of the nuclear magnetic resonance (NMR) flux meter used to measure the magnetic field. Since the ions are of constant mass (126.94 amu for Iodine and 78.93, 80.93 amu for Bromine) and the charges must be integral multiples of the electronic charge, the magnet selects from the continuous spectrum of ion energies groups of ions of constant E/q^2. The result is a spectrum of sharp peaks such as shown in Figures 9 and 10. Solving the magnet equation for $E = q^2\nu^2k/M$, shows how the identification of the charge state of a given peak, along with knowledge of the constant, k, allows one to determine the energy associated with that peak (ν and M are, of course, known for a given run).

The magnet constant, k, was determined by a reverse threshold run of the reaction $O^{16} + d = >F^{17} + n$. O^{16} was used to bombard a deuterium target. The threshold energy for the reaction, E_{th}, is calculated and the magnet equation solved for $k = \frac{E_{th}M}{\nu_{th}^2 q^2}$. The threshold NMR frequency is determined experimentally by making runs at several frequencies and detecting the neutrons given off in the reaction. The experiment was done for deuterium bombarded with both O^{3+} and O^{4+}, giving two independent determinations of k. The two values differed by 0.056 per cent and the average of the two was used.

The charge states of the peaks were determined by the use of two runs, one at NMR frequency, ν_1, and the other at higher frequency,

ν_2. Two peaks, of charge q_1 and next higher charge q_2 are chosen from the lower value run. These peaks occur at pulse-heights x_1^1 and x_1^2, respectively. A peak with charge state q_1 and occurring at pulse-height, x_2^1 is chosen from the second run. Now, the assumption is required that the energy of an ion of given mass and the pulse-height obtained with a surface barrier detector are linearly related, i.e., $E = ax + b$. The validity of this assumption is indicated by results of this work (see Figure 16).

For the peak at x_1^1 we may write;

$$ax_1^1 + b = \frac{kq_1^2\nu_1^2}{M} \tag{1}$$

and for the peak at x_1^2;

$$ax_1^2 + b = \frac{kq_2^2\nu_1^2}{M} \tag{2}$$

Subtracting (1) from (2);

$$a(x_1^2 - x_1^1) = \frac{k}{M}\nu_1^2(q_2^2 - q_1^2) \tag{3}$$

Writing the equation for the peak at x_2^1 and subtracting (1) from it yields;

$$a(x_2^1 - x_1^1) = \frac{k}{M}q_1^2(\nu_2^2 - \nu_1^2) \tag{4}$$

Finally, the ratio of (4) to (3) is;

$$\frac{x_1^2 - x_1^1}{x_2^1 - x_1^1} = \frac{\nu_1^2}{\nu_2^2 - \nu_1^2}\left(\frac{q_2^2}{q_1^2} - 1\right) \tag{5}$$

The right side of (5) is tabulated for values of q from q = 12 to q = 20. Two adjacent peaks are chosen from the lower frequency run (x_1^1 and x_1^2) and by trial and error, x_2^1 is found. All other peaks in the runs serve as checks.

The identification of the charge states of the peaks in a given run associates an energy and a velocity with each peak. These energies and velocities are determined by the magnetic analysis of the ions and may, therefore, be related to the pulse-heights obtained from solid-state detectors or time-to-pulse converters in such a way as to calibrate these devices.

APPENDIX B

RESPONSE OF ZERO DETECTOR AS A FUNCTION OF FISSION FRAGMENT ENERGY AND VELOCITY

The zero of time detection system has been described previously and the electron lens is shown in Figure 2. In order to determine the dependence of the signal amplitude of the zero detector on fission fragment energy and velocity, the output signal was recorded in correlation with energy and with time-of-flight measurements on fission fragments.

In addition to the fast timing signal, the 14 stage photomultiplier in the zero detector is wired such that a signal may be taken off the 10th dynode. This signal was amplified by an ORNL A-1 linear amplifier system and recorded on one side of a two parameter, 256 x 256, correlation analyzer. On the other side was recorded the pulse-height distribution associated with the energy, or with the time-of-flight of fission fragments from the thermal neutron induced fission of ^{235}U.

The results of these measurements are shown in Figures 33a through 33f. The flags are statistical. Figures 33a and 33d show the zero signal amplitude distribution for fission fragments with the full range of energies and times-of-flight, respectively. Figures 33b and 33e show the distributions only for those fission fragments that have energies and times-of-flight, respectively, that occur directly under the high energy peak. In Figures 33c and 33f the same is true for the low energy peak. There is apparently no significant dependence of the zero signal amplitude on fission fragment energy or velocity.

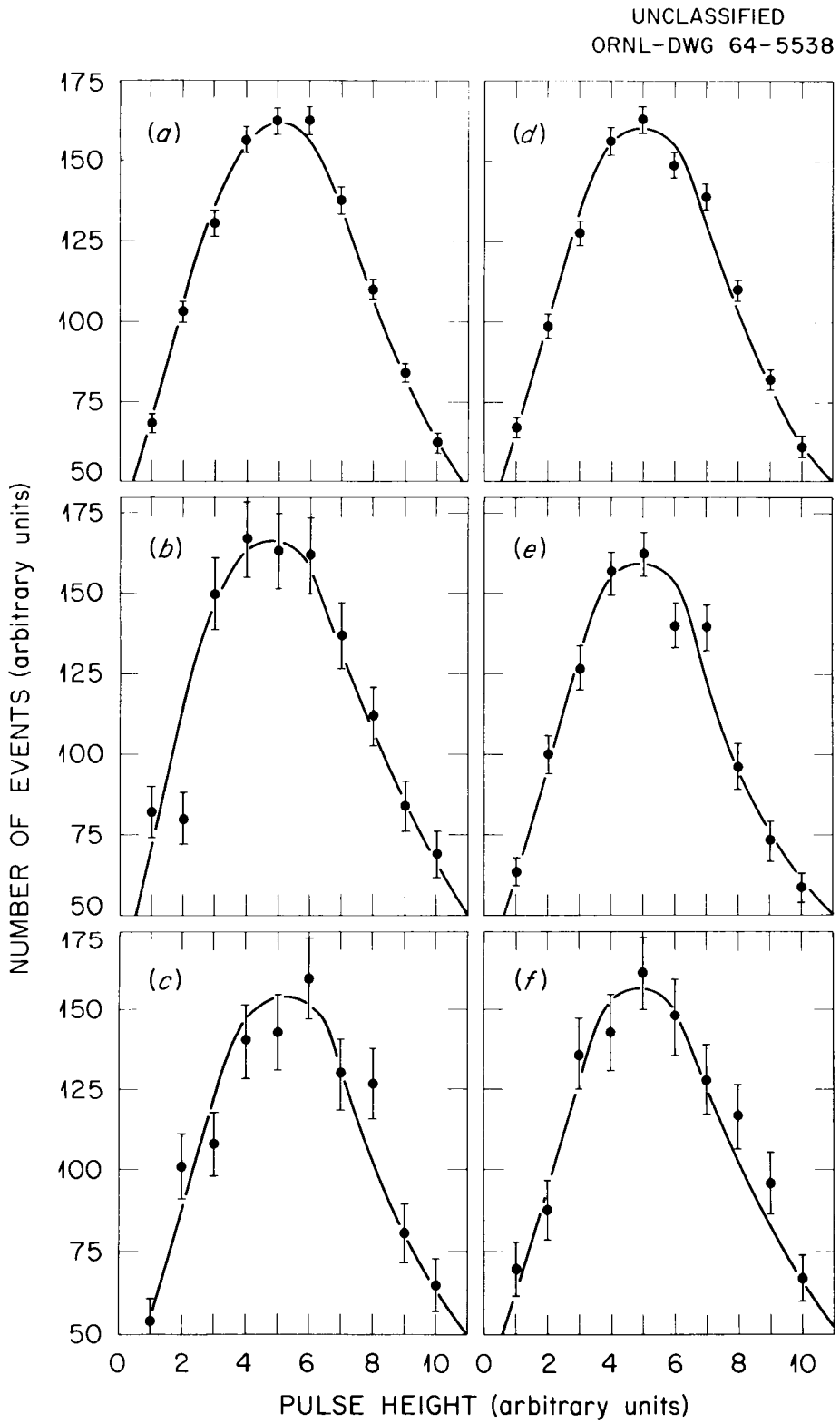

Figure 33. Response of Zero Detector to Fission Fragments of Various Energies and Velocities.

APPENDIX C

CORRECTING EXPERIMENTAL DATA FOR INSTRUMENTAL RESOLUTION*

Let $F(x)$ be a measured experimental distribution function. Then if the instrumental resolution function of the system is Gaussian,

$$F(x_o)\Delta x_o = \sum_{i=-\infty}^{\infty} I(x_i)\Delta x_i \frac{1}{\sqrt{2\pi\sigma_i^2}} \exp\left[-\frac{(x_i - x_o)^2}{2\sigma_i^2}\right] \Delta x_o, \qquad (1)$$

where $I(x)$ is the distribution for infinitely good resolution and Δx_o is any interval in x with $\Delta x_{-i} \ldots \Delta x_i$ the adjacent intervals. Now if $I(x_i)$ is expanded about $x_i = x_o$,

$$I(x_i) = I(x_o) + (x_i - x_o)I'(x_o) + \frac{(x_i - x_o)^2}{2} I''(x_o) + \ldots \qquad (2)$$

Substitution (2) in (1),

$$F(x_o)\Delta x_o = I(x_o)\Delta x_o \sum_{i=-\infty}^{\infty} \frac{1}{\sqrt{2\pi\sigma_i^2}} \exp\left[-\frac{(x_i - x_o)^2}{2\sigma_i^2}\right] \Delta x_i$$

$$+ I'(x_o)\Delta x_o \sum_{i=-\infty}^{\infty} \frac{x_i - x_o}{\sqrt{2\pi\sigma_i^2}} \exp\left[-\frac{(x_i - x_o)^2}{2\sigma_i^2}\right] \Delta x_i \qquad (3)$$

$$+ I''(x_o)\Delta x_o \sum_{i=-\infty}^{\infty} \frac{(x_i - x_o)^2}{2!\sqrt{2\pi\sigma_i^2}} \exp\left[-\frac{(x_i - x_o)^2}{2\sigma_i^2}\right] \Delta x_i + \ldots$$

---

*The following development is due to Dr. H. W. Schmitt of the Oak Ridge National Laboratory.

Making the assumption that σ is a constant, the odd terms sum to zero. (In this work σ was a slowly varying linear function of the variable.) Also, in the limit,

$$\sum_{i=-\infty}^{\infty} \frac{1}{\sqrt{2\pi\sigma^2}} \exp\left[-\frac{(x_i - x_o)^2}{2\sigma^2}\right]\Delta x_i \Rightarrow \int_{-\infty}^{\infty} \frac{1}{\sqrt{2\pi\sigma^2}} \exp\left[-\frac{(x_i - x_o)^2}{2\sigma^2}\right] dx = 1.$$

Assuming that all of the derivatives greater than the second are negligible, then,

$$F(x_o)\Delta x_o = I(x_o)\Delta x_o + I''(x_o)\Delta x_o \int_{-\infty}^{\infty} \frac{(x_i - x_o)^2}{2!\sqrt{2\pi\sigma^2}} \exp\left[-\frac{(x_i - x_o)^2}{2\sigma^2}\right] dx.$$

The integration can be done by parts to yield $\sigma^2/2$. Therefore,

$$F(x) = I(x) + \frac{\sigma^2}{2}\frac{d^2I}{dx^2}, \quad \text{or}$$
$$I(x) = F(x) - \frac{\sigma^2}{2}\frac{d^2I(x)}{dx^2}. \qquad \text{(A-1)}$$

However, the function available is $F(x)$, not $I(x)$, so the further assumption is necessary that the resolution of the system does not drastically alter the curvature of the distribution and $\frac{d^2I}{dx^2} \approx \frac{d^2F}{dx^2}$. While this last assumption might not be a very good one, in practice it causes no great difficulty because the resolution can be unfolded in a series of iterative calculations giving, finally, $I(x)$ rigorously from Eq. (A-1).

ORNL-3692
UC-34 — Physics
TID-4500 (32nd ed.)

INTERNAL DISTRIBUTION

1. Biology Library
2-4. Central Research Library
5. Reactor Division Library
6-7. ORNL — Y-12 Technical Library Document Reference Section
8-57. Laboratory Records Department
58. Laboratory Records, ORNL R.C.
59. J. A. Biggerstaff
60. J. L. Blankenship
61. G. E. Boyd
62-63. R. L. Ferguson
64. J. L. Fowler
65-66. Glen Gordon
67. R. L. Hahn
68. C. E. Larson
69. P. D. Miller
70. F. L. Moore
71. F. Pleasonton
72. H. W. Schmitt
73. M. J. Skinner
74. A. H. Snell
75. J. A. Swartout
76. A. M. Weinberg
77. A. M. Clogston (consultant)
78. B. L. Cohen (consultant)
79. M. Deutsch (consultant)
80. D. L. Judd (consultant)
81. L. J. Rainwater (consultant)
82. J. A. Wheeler (consultant)

EXTERNAL DISTRIBUTION

83-92. W. E. Kiker, Lawrence Radiation Laboratory, Livermore
93. R. D. Present, University of Tennessee, Knoxville
94. V. B. Bhanot, Physics Department, Panjab University, Chandigarh-3, India
95. Research and Development Division, AEC, ORO
96-739. Given distribution as shown in TID-4500 (32nd ed.) under Physics category (75 copies — OTS)